J. Fluid Mech. (2022), *vol*. 939, A3, doi:10.1017/jfm.2022.138

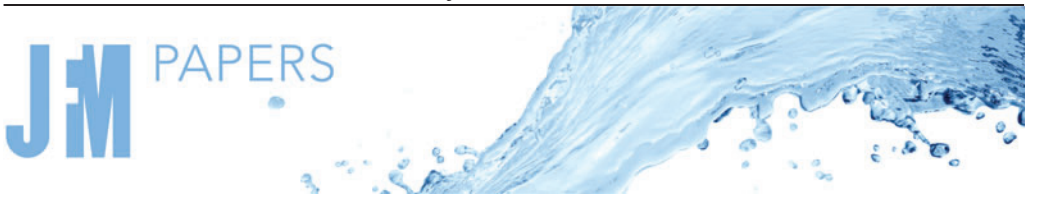

Internal shear layers in librating spherical shells: the case of periodic characteristic paths

Jiyang He[1],†, **Benjamin Favier**[1], **Michel Rieutord**[2] **and Stéphane Le Dizès**[1]

[1]Aix Marseille Univ, CNRS, Centrale Marseille, IRPHE, F-13384 Marseille, France

[2]IRAP, Université de Toulouse, CNRS, UPS, CNES, 14 avenue Édouard Belin, F-31400 Toulouse, France

(Received 13 September 2021; revised 5 January 2022; accepted 9 February 2022)

Internal shear layers generated by the longitudinal libration of the inner core in a spherical shell rotating at a rate Ω^* are analysed asymptotically and numerically. The forcing frequency is chosen as $\sqrt{2}\Omega^*$ such that the layers issued from the inner core at the critical latitude in the form of concentrated conical beams draw a simple rectangular pattern in meridional cross-sections. The asymptotic structure of the internal shear layers is described by extending the self-similar solution known for open domains to closed domains where reflections on the boundaries occur. The periodic ray path ensures that the beams remain localised around it. Asymptotic solutions for both the main beam along the critical line and the weaker secondary beam perpendicular to it are obtained. The asymptotic predictions are compared with direct numerical results obtained for Ekman numbers as low as $E = 10^{-10}$. The agreement between the asymptotic predictions and numerical results improves as the Ekman number decreases. The asymptotic scalings in $E^{1/12}$ and $E^{1/4}$ for the amplitudes of the main and secondary beams, respectively, are recovered numerically. Since the self-similar solution is singular on the axis, a new local asymptotic solution is derived close to the axis and is also validated numerically. This study demonstrates that, in the limit of vanishing Ekman numbers and for particular frequencies, the main features of the flow generated by a librating inner core are obtained by propagating through the spherical shell the self-similar solution generated by the singularity at the critical latitude on the inner core.

Key words: boundary layer separation, waves in rotating fluids

1. Introduction

In astrophysical fluid bodies, such as metallic liquid cores and subsurface oceans, complex fluid flows can be excited by mechanical forcing (Le Bars, Cébron & Le Gal 2015). Libration, precession and tides, which correspond to harmonic perturbations of the

† Email address for correspondence: he@irphe.univ-mrs.fr

rotation rate, rotation axis and body shape, respectively, are the most common large-scale forcings originating from gravitational interactions between orbiting bodies. Libration in particular is crucial for quasi-synchronised bodies locked in a spin–orbit resonance with their orbiting companion. The amplitude of the response to libration forcing helps constrain the internal structure of astrophysical bodies, indicating, for example, the existence of a subsurface ocean in Enceladus (Thomas *et al.* 2016). The internal flows driven by such forcing have been extensively studied both numerically (Calkins *et al.* 2010; Cébron *et al.* 2012; Favier *et al.* 2015) and experimentally (Noir *et al.* 2009, 2012; Grannan *et al.* 2014; Le Reun, Favier & Le Bars 2019).

In a rotating fluid, the Coriolis acceleration acts as a restoring force leading to the propagation of inertial waves whose frequency ω^* is smaller than twice the rotation rate Ω^* (Greenspan 1968). In closed geometries, propagating inertial waves can eventually form global modes which can be resonantly excited by an external forcing (Aldridge & Toomre 1969). While analytical inviscid solutions exist for simple geometries such as the cylinder or the sphere, the ill posedness of the inviscid problem in a closed domain implies that singularities are the norm rather than the exception. Even when inviscid modes exist, such as for the cylinder, viscous corrections at the corners tend to spawn internal shear layers (McEwan 1970). In a spherical shell, two types of inviscid singularities are observed. Attractors are formed by the gradual convergence of characteristics along which inertial-wave beams propagate (Rieutord, Georgeot & Valdettaro 2001; Rieutord & Valdettaro 2018). A second type of singularity appears wherever the boundary is locally tangent to the direction of propagation of inertial waves, the so-called critical latitude (Kerswell 1995). Viscosity naturally regularises these inviscid attractors and the singular surfaces associated with critical latitudes, which gives rise to different types of internal shear layers propagating in the bulk of the rotating fluid. These shear layers are also relevant to stratified fluids, which can support internal gravity waves that are very similar at the linear level with inertial waves in rotating fluids. Internal and inertial attractors have been experimentally found in a rectangular basin with one sloping boundary by Maas *et al.* (1997) and Manders & Maas (2003), respectively. The internal shear layers spawned by critical latitudes on concave and convex boundaries have also been observed experimentally in a precessing spheroid (Noir *et al.* 2001) and librating (spherical and ellipsoidal) shells (Koch *et al.* 2013; Lemasquerier *et al.* 2017), respectively. They could play an important role in the mixing of stratified fluids (Brouzet *et al.* 2016; Dauxois *et al.* 2018) and the generation of zonal flows in rapidly rotating fluid bodies (Maas 2001; Morize *et al.* 2010; Favier *et al.* 2014; Le Dizès 2015).

The dependence of oscillating internal shear layers on frequency has been tackled both as eigenvalue (Rieutord & Valdettaro 1997; Rieutord *et al.* 2001; Rieutord, Valdettaro & Georgeot 2002; Rieutord & Valdettaro 2018) and forced problems (Ogilvie 2009; Rieutord & Valdettaro 2010; Lin & Ogilvie 2018, 2021). Eigenmodes computed with the first approach are categorised as attractors, critical-latitude and quasi-regular modes based on the path of characteristics (Rieutord & Valdettaro 2018). For the forced problem, the response is classified as resonant, non-resonant or anti-resonant when its dissipation increases, remains constant or vanishes as viscosity tends to zero (Rieutord & Valdettaro 2010). The anti-resonant response occurs at the frequencies of periodic orbits. The non-resonant counterpart is observed at the frequencies of attractor modes, while the resonant one corresponds to the frequencies where global modes are hidden beneath the localised wave beams (Lin & Ogilvie 2021).

There are numerous theoretical and numerical studies investigating the scaling laws of oscillating internal shear layers. It is now accepted that the width of the shear layers

spawned from the critical latitude scales like $E^{1/3}$ (Walton 1975*b*; Kerswell 1995), where E is the Ekman number measuring the importance of viscosity compared with rotational effects. Such a scaling has been demonstrated in several numerical works (Favier *et al.* 2014; Lin & Noir 2021). However, the scaling for the amplitude of the response is disputed in the literature. Early theoretical predictions by Kerswell (1995) asserted that the strength of the internal shear layers spawned from the inner boundary in a spherical shell should follow a $E^{1/6}$ scaling, which is also observed numerically (Calkins *et al.* 2010; Favier *et al.* 2014; Cébron *et al.* 2019). However, by asymptotically matching the solution of the internal shear layer to that of the boundary layer near the critical latitude, Le Dizès & Le Bars (2017) found that the amplitude should scale with $E^{1/12}$. Recent numerical results by Lin & Noir (2021) at Ekman numbers in the range $10^{-7} < E < 10^{-5}$, namely at lower viscosities than previous work, tend to favour the scaling $E^{1/12}$ over $E^{1/6}$. In the present paper, we will further validate the amplitude scaling $E^{1/12}$ by reaching Ekman numbers as low as $E = 10^{-10}$.

One of the difficulties associated with these internal shear layers is their behaviour as they bounce on solid boundaries. Moore & Saffman (1969) and Thomas & Stevenson (1972) introduced self-similar solutions to describe the wave beams in unbounded geometries for rotating and stratified fluids, respectively. These similarity solutions are leading-order expressions describing the viscous smoothing in a $O(E^{1/3})$ layer of a local inviscid singularity propagating along a characteristic line. Le Dizès & Le Bars (2017) applied these solutions to the case of the critical-latitude singularity on a librating axisymmetric convex surface. They also numerically demonstrated the ability of the self-similar solutions to describe the internal shear layers generated by a librating spheroid in an unbounded domain. In a bounded domain, such as a spherical shell, where reflections on the boundaries and attractor singularities exist, the similarity solutions were found to be able to describe the internal shear layers created by the critical-latitude singularity (Walton 1975*a*) and attractors (Rieutord *et al.* 2001; Ogilvie 2005). Internal shear layers are wave packets. How these wave packets are reflected on the boundaries depends on the geometry of the reflecting surfaces. On a flat surface, they are completely reflected, as plane waves, in a characteristic direction different from the incident one (Phillips 1963, 1966; Kistovich & Chashechkin 1994; Le Dizès 2020), while on a curved surface there may exist 'back-reflected' waves along the incident characteristic but in the opposite direction (Baines 1971*a*). Moreover, when the incident characteristic is tangent to the curved surface at some point, the incident waves are also split into two different waves (Baines 1971*b*). However, in both cases, if the wavelengths of the incident beam are sufficiently large compared with the length scales of the reflecting surface, the back-reflected response is negligible (Baines 1971*a*). We shall be in this situation in the present study.

In this paper, we consider the inertial waves generated by the longitudinal libration of the inner core of a rotating spherical shell in the linear limit of infinitesimal forcing amplitudes and Ekman numbers. The objective is to generalise the work of Le Dizès & Le Bars (2017) to the case of a closed geometry involving reflections on curved solid boundaries. For simplicity, we do not consider the case of attractors and focus on the shear layer spawned from the critical latitude at a particular frequency for which the characteristic path eventually comes back to the critical latitude after several reflections. These periodic orbits (Rieutord *et al.* 2001; Rieutord & Valdettaro 2018) are a natural choice since the path of characteristics remains topologically simple, which would not be the case for frequencies sustaining attractors. For illustration, the shear layers in a spherical shell forced by the libration of the inner core are displayed in figure 1. This solution is obtained by the direct numerical integration of the linearised viscous equations and will serve as a reference to

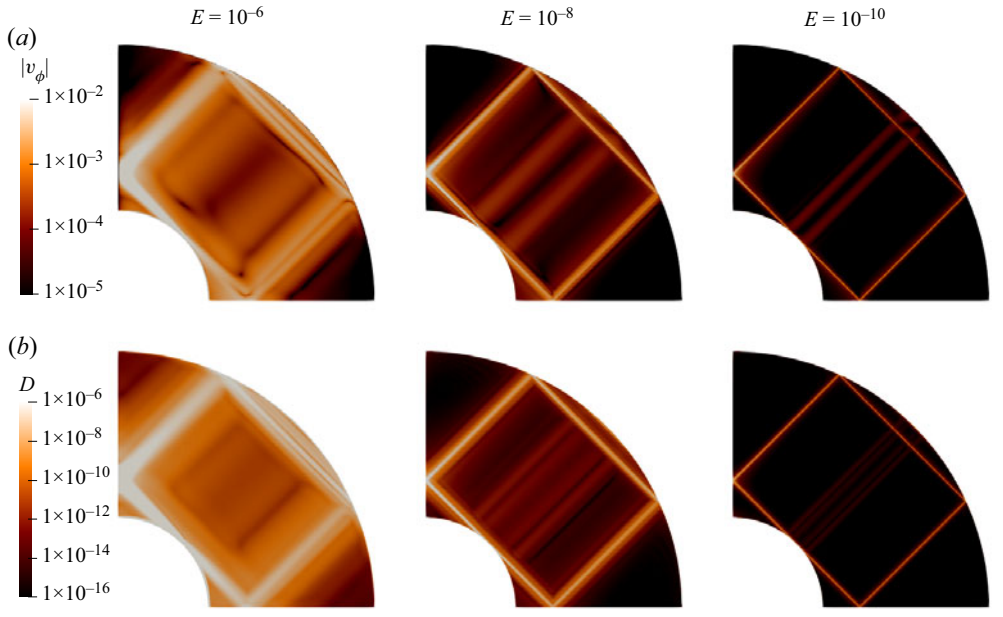

Figure 1. Contours of the amplitude of azimuthal velocity $|v_\phi|$ (a) and dissipation D (b) for three Ekman numbers obtained by the direct numerical integration of the linear forced viscous problem. The aspect ratio of the spherical shell is $\eta = 0.35$ and the dimensionless librating frequency of the inner core is $\omega = \sqrt{2}$.

which the generalised asymptotic solution introduced in this paper will be systematically compared.

The paper is organised as follows. Section 2.1 introduces the setting of the problem and the basic equations. Then we describe the asymptotic theory in § 2.2. The self-similar solution in an open geometry and its scaling are recalled in § 2.2.1. In § 2.2.2, we recall the reflection laws on a flat boundary and on the axis. The extended asymptotic solutions for different regions of the spherical shell are derived in §§ 2.2.3–2.2.4. Section 2.3 is devoted to the description of the numerical method used to integrate the linearised equations. The comparison between the theoretical predictions and the numerical results is performed in § 3 for the solution in the bulk. Close to the axis, the self-similar solution is singular. In § 4, a new asymptotic solution valid close to the axis is derived using Hankel transforms and compared with the numerical solution. Finally, a summary and possible directions for future works are discussed in § 5.

2. Framework

2.1. *Basic equations*

We consider the viscous incompressible rotating flow filling a spherical shell and forced by the libration of the inner core, as shown in figure 2. The radii of the outer and inner spheres are ρ^* and $\eta\rho^*$ (with $0 < \eta < 1$), respectively. The flow between them rotates around the symmetry axis Oz and with an angular velocity Ω^* . The inner core librates at an amplitude ε^* and frequency ω^*, such that the corresponding angular rotation rate is $\Omega^* + \varepsilon^* \cos(\omega^* t^*)$. Space and time variables are non-dimensionalised by the outer radius ρ^* and angular period $1/\Omega^*$, respectively. The non-dimensional radii of the outer and inner shells are then 1 and η, respectively, while the non-dimensional angular velocity of

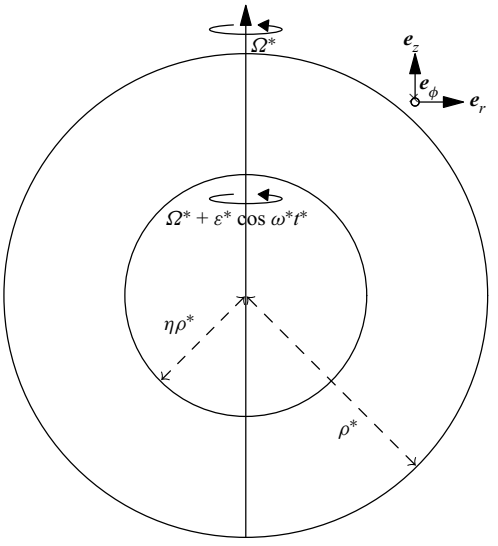

Figure 2. Schematic of the problem: the outer shell of radius ρ^* rotates with an angular velocity Ω^*, while the inner one of radius $\eta\rho^*$ rotates at $\Omega^* + \varepsilon^* \cos(\omega^* t^*)$ with ε^* and ω^* being the amplitude and frequency of the libration, respectively.

the inner core is $1 + \varepsilon \cos \omega t$ with libration amplitude $\varepsilon = \varepsilon^*/\Omega^*$ and libration frequency $\omega = \omega^*/\Omega^*$. The Ekman number is defined by

$$E = \frac{\nu}{\Omega^* \rho^{*2}}, \tag{2.1}$$

with ν being the kinematic viscosity.

Since we are concerned with the harmonic linear response in the limit of small viscosity, both the libration amplitude and the Ekman number are assumed to be small. The libration frequency ω is chosen in the inertial-wave range such that it can be written as $\omega = 2 \cos \theta_c$. The angle θ_c indicates the direction of propagation of the inertial waves with respect to the equatorial plane. It also corresponds to the inclination angle that internal shear layers make with respect to this plane. In order to form a simple closed circuit, θ_c is fixed to 45°. This means that the libration frequency ω is fixed to $\sqrt{2}$. These values are unchanged throughout the paper. An example of the ray path is shown in figure 3, where the internal shear layer is initially spawned at the critical latitude S_c and returns to it after bouncing on the axis, reflecting twice on the outer boundary and reflecting on the equatorial plane, thanks to the imposed symmetry.

The flow is governed by the linearised incompressible Navier–Stokes equations in the rotating frame. We seek the following harmonic solution for the velocity $\boldsymbol{V}$ and pressure P

$$(\boldsymbol{V}, P) = \varepsilon(\boldsymbol{v}, p)\, \mathrm{e}^{-\mathrm{i}\omega t} + \text{c.c.}, \tag{2.2}$$

where the notation c.c. denotes complex conjugate terms. The velocity $\boldsymbol{v}$ and pressure p satisfy the following equations in the rotating frame

$$-\mathrm{i}\omega \boldsymbol{v} + 2\boldsymbol{e}_z \times \boldsymbol{v} = -\boldsymbol{\nabla} p + E\nabla^2 \boldsymbol{v}, \tag{2.3a}$$

$$\boldsymbol{\nabla} \cdot \boldsymbol{v} = 0, \tag{2.3b}$$

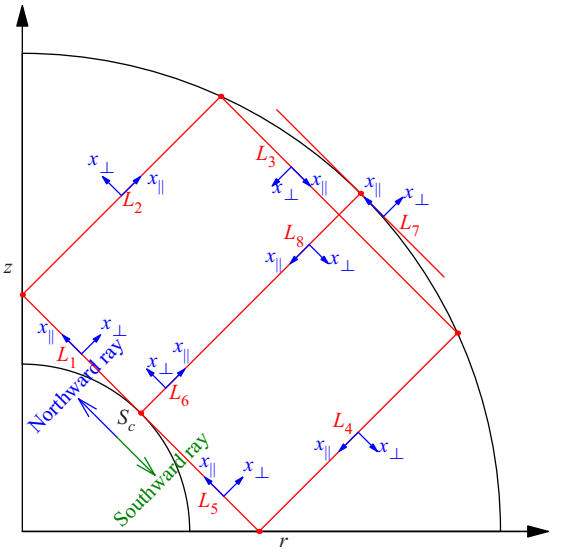

Figure 3. Critical lines L_j ($j = 1, 2 \ldots 8$) and the local coordinate systems $(x_\parallel, x_\perp)$ for rays initially emitted in the northward direction. The opposite directions are used for rays initially emitted in the southward direction.

with the boundary conditions

$$\boldsymbol{v} = r\boldsymbol{e}_\phi \quad \text{on the inner shell,} \tag{2.4a}$$

$$\boldsymbol{v} = \boldsymbol{0} \quad \text{on the outer shell,} \tag{2.4b}$$

where r is the distance to the rotation axis.

2.2. *Asymptotic theory*

The asymptotic analysis is conducted within the cylindrical coordinate system (r, z, ϕ). The basic idea of the asymptotic theory is to assume that the main features of the solution come from the propagation of the critical-latitude singularity S_c localised at $r = \eta\sqrt{1-\omega^2/4}$ and $z = \eta\omega/2$ on the inner sphere. For the frequency $\omega = \sqrt{2}$, this singularity is expected to propagate along the critical characteristic lines L_j ($j = 1 \ldots 8$) and form a closed circuit (see figure 3). The northward rays correspond to the rays initially propagating along the line L_1. They then cover the circuit $L_1 \to L_2 \to L_3 \to L_4 \to L_5$, possibly bounce on the inner core leading to the additional path $L_6 \to L_7 \to L_8$ before starting the circuit again. Similarly, the southward rays start propagating on the line L_5 from S_c, travelling on $L_5 \to L_4 \to L_3 \to L_2 \to L_1$ (possibly on $L_8 \to L_7 \to L_6$) and continuing the same circuit again. The critical lines L_1–L_5 correspond to the main beam (inclined quadrilateral) observed in figure 1, while L_6–L_8 are responsible for the two secondary wider and weaker beams near the centre line $z = r$. Both northward and southward rays are expected to contribute to the solution. Note, however, that computing their contribution will require considering their interaction with the rotation axis and their reflections on boundaries.

For building the asymptotic solution around these critical lines, it is useful to introduce a local frame $(x_\parallel, x_\perp)$ for each critical line where $x_\perp = 0$ corresponds to the critical line itself. The variable $x_\parallel$ measures the travelled distance from the source along the critical lines. It increases as the ray propagates on each critical line. However, as we shall see

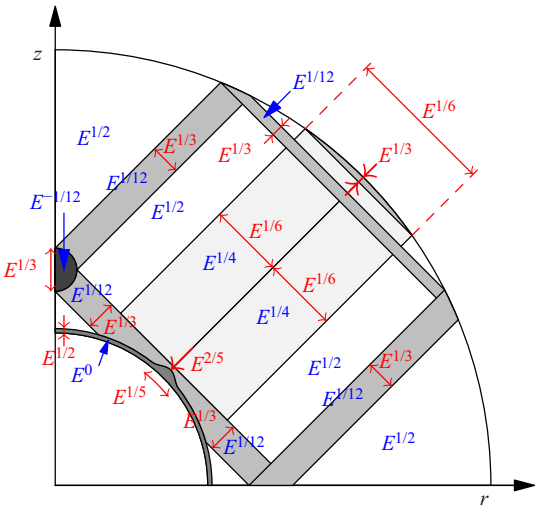

Figure 4. Ekman scalings in a spherical shell: length scales and amplitudes are shown in red and blue, respectively.

below, it may exhibit a jump when the ray is reflected. The variable $x_\perp$ indicates the position with respect to the critical line. The orientation of $x_\perp$ can *a priori* be arbitrarily chosen. For convenience, we have assumed that the orientation does not change sign during the propagation, that is a ray at a positive $x_\perp$ stays at a positive $x_\perp$ after reflection. The orientation of the local frames shown in figure 3 is for the northward rays. Opposite local frames are taken for the southward rays.

The final result of the asymptotic analysis in terms of Ekman scalings is summarised in figure 4. The Ekman layer adjacent to the inner core is characterised by a $E^{1/2}$ width and a E^0 velocity amplitude. Around the critical latitude the width increases to $E^{2/5}$ with an extension of $E^{1/5}$ along the boundary (Roberts & Stewartson 1963). The width and the amplitude of the main beams around the critical lines L_1–L_5 are of order $E^{1/3}$ and $E^{1/12}$, respectively (see § 2.2.3), while those of the secondary beams around L_6 and L_8 are of order $E^{1/6}$ and $E^{1/4}$, respectively (see § 2.2.4). Near L_7, the beam recovers the $E^{1/3}$ width of the main beam, while it travels a distance of order $E^{1/6}$ along L_7. Around the axis where two main beams intersect, the length scale remains as $E^{1/3}$, while the amplitude diverges as $E^{-1/12}$ (see § 4).

2.2.1. *Self-similar solution and scaling*

As first shown by Moore & Saffman (1969), the propagation and viscous smoothing of a localised singularity can be described in the limit of small Ekman numbers by a self-similar solution. This result has been used and applied to the critical-latitude singularity generated by the libration of a sphere in Le Dizès & Le Bars (2017). We now briefly recall the main results.

The self-similar form is derived by considering the small Ekman number limit of the governing equations projected onto the local frame $(x_\parallel, x_\perp)$. The solution is characterised by $v_\parallel$, $v_\perp$, v_ϕ and p. The former two are velocity components along and perpendicular to the critical lines, while the latter two correspond to the azimuthal velocity and pressure, respectively. As the width of the internal shear layer regularised by viscosity scales with $E^{1/3}$, all quantities are expanded with the perturbation parameter $E^{1/3}$. The dependence

on the radial coordinate r is removed by dividing the solution by $\sqrt{r}$. At leading order, only $v_\parallel$ and v_ϕ are required to fully describe the solution. The former has the following self-similar form:

$$v_\parallel = \frac{1}{\sqrt{r}} C_0 H_m(x_\parallel, \zeta) = \frac{1}{\sqrt{r}} C_0 \left(\frac{x_\parallel}{2\sin\theta_c} \right)^{-m/3} h_m(\zeta), \tag{2.5}$$

with the similarity variable

$$\zeta = x_\perp E^{-1/3} \left(\frac{2\sin\theta_c}{x_\parallel} \right)^{1/3}, \tag{2.6}$$

and the function

$$h_m(\zeta) = \frac{\mathrm{e}^{-\mathrm{i}m\pi/2}}{(m-1)!} \int_0^{+\infty} \mathrm{e}^{\mathrm{i}p\zeta - p^3} p^{m-1}\, \mathrm{d}p. \tag{2.7}$$

The real index m and the complex amplitude C_0 are the parameters characterising the strength and the (complex) amplitude of the singularity. Expression (2.5) is a leading-order expression of a viscous solution in the limit of small Ekman numbers. Next-order corrections are expected to be $O(E^{1/3})$. The solution preserves the self-similar structure described by $h_m(\zeta)$ during its propagation and decay as $x_\parallel^{-m/3}$ with $x_\parallel$ being the distance from the source. Note that there are two singularities in (2.5). One is on the rotation axis where $r = 0$, the other is at the source $x_\parallel = 0$. The similarity solution requires modification close to these two regions. In addition, it is modified close to the boundaries where the solution should be derived following the more classical $E^{1/2}$ scaling characteristic of Ekman viscous layers (see Le Dizès 2020).

Le Dizès & Le Bars (2017) derived the particular values of the two parameters m and C_0 for any axisymmetric convex librating object by matching the similarity solution with the boundary layer solution close to the critical latitude. As a necessary condition for matching, they obtained the particular values

$$m = 5/4, \tag{2.8}$$

and

$$C_0 = \frac{E^{1/12}}{8(2\sin\theta_c)^{3/4}} \mathrm{e}^{\mathrm{i}\pi/2} \quad \text{for a northward ray,} \tag{2.9a}$$

$$C_0 = \frac{E^{1/12}}{8(2\sin\theta_c)^{3/4}} \mathrm{e}^{\mathrm{i}3\pi/4} \quad \text{for a southward ray.} \tag{2.9b}$$

The curvature at the critical latitude $\kappa_c = -\sin\theta_c$ for the spherical inner core has been applied. Note that there is an error concerning the phase of C_0 in Le Dizès & Le Bars (2017), which is corrected here. The value $m = 5/4$ implies that the ray amplitude decays as $x_\parallel^{-5/12}$. The parameters C_0 for the northward and southward rays only differ by a phase shift of $\pi/4$. These two values of C_0 only hold for the initial rays directly spawned from the source. For the subsequent reflected rays, the phase and amplitude of C_0 have to be modified as they will be in the next subsection.

The relation between the azimuthal velocity v_ϕ and the parallel velocity $v_\parallel$ is

$$v_\phi = \pm \mathrm{i} v_\parallel. \tag{2.10}$$

The sign depends on the angle between the local unit vector $\boldsymbol{e}_\parallel$ and the global unit vector $\boldsymbol{e}_r$. The $+$ sign is taken for obtuse angles, while the $-$ sign is taken for acute ones.

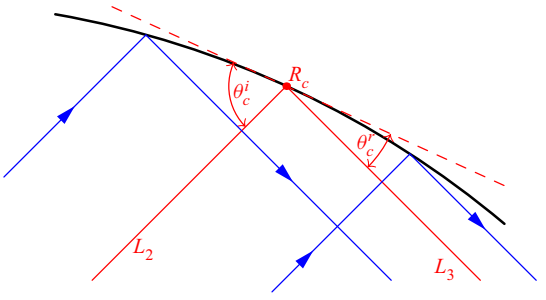

Figure 5. Reflection on the outer boundary from the incident beam around L_2 to the reflected beam around L_3: red and blue solid lines are critical lines and wave beams, respectively; the red dashed line is the tangent plane at the reflection point R_c; θ_c^i and θ_c^r are the incident and reflected angles.

The values (2.9*a*,*b*) of C_0 clearly show that the amplitude of the leading-order asymptotic solution scales with $E^{1/12}$. Numerical results in open and closed geometries have partially confirmed such scaling at relatively high Ekman numbers (above 10^{-7}) (Le Dizès & Le Bars 2017; Lin & Noir 2021). Further evidence about this scaling at lower Ekman numbers will be provided here.

2.2.2. *Reflections on the outer boundary and on the axis*

As shown in figure 3, there are two reflections ($L_2 \to L_3$ and $L_3 \to L_4$) on the outer boundary. How the incident beam reflects on the curved boundary depends on its relative length scales compared with those of the reflecting surface. As proved by Baines (1971*a*) for a plane wave, the 'back-reflected' wave along the incident characteristic but in the opposite direction vanishes when the incident wavenumber becomes large, and the incident wave feels the curved boundary as locally flat and reflects as a local plane wave on a flat surface. For our case, the wave beam described by the similarity solution (2.5) is shown to be dominated by large wavenumbers (see Appendix A). Therefore, the possible 'back-reflected' wave beam is negligible and not considered, as shown in the figure 5 for the reflection of an incident beam along L_2 yielding only a reflected beam along L_3. Moreover, the reflection on the curved boundary can be approximated by that on the flat tangent surface at the critical reflection point R_c (in red dashed line).

The reflection of internal shear layers on a flat boundary has been studied by Le Dizès (2020). The incident and reflected wave beams were found to preserve, at leading order, their self-similar structures, which are

$$v_\parallel^i = C_0^i H_m(x_\parallel^i, \zeta^i)/\sqrt{r}, \quad v_\parallel^r = C_0^r H_m(x_\parallel^r, \zeta^r)/\sqrt{r}, \tag{2.11a,b}$$

where the superscripts i and r denote the variables associated with the incident and reflected beams, respectively. The corresponding reflection laws take the forms

$$\frac{x_{\parallel c}^i}{x_{\parallel c}^r} = K^3, \quad \frac{C_0^i}{C_0^r} = K^{m-1}, \tag{2.12a,b}$$

with $K = \sin\theta_c^i / \sin\theta_c^r$ the ratio of the sines of the critical incident and reflected inclination angles θ_c^i and θ_c^r. Here, $x_{\parallel c}^i$ and $x_{\parallel c}^r$ are the distances between the critical reflection point R_c and the source before and after the reflection, respectively. The above reflection laws suggest that the effective source is displaced and the amplitude is modified by the reflection on the flat boundary. The reflected beam appears to be generated from a 'virtual' source

located at the position $x_{\parallel}^{r}$ away from the reflection point R_c and with a strength C_0^r. Note that K is a real number, so the phase is left unchanged by the reflection on the boundary. It is worth mentioning that viscous corrections are also created during the reflection process. These corrections are not considered in the present work. Le Dizès (2020) has shown that they are $O(E^{1/6})$ smaller and also possess a self-similar structure.

The reflection on the axis from L_1 to L_2 (see figure 3) has been discussed by Le Dizès & Le Bars (2017) and Rieutord & Valdettaro (2018), which reveals that the phase of the parallel velocity is shifted by $\pi/2$ while the amplitude and the distance to the source is kept the same. By the same method, the reverse reflection from L_2 to L_1 also shifts the phase of the parallel velocity by $\pi/2$ while keeping all other quantities unchanged. In other words, we always have on the axis

$$C_0^r = \mathrm{e}^{\mathrm{i}\pi/2} C_0^i. \tag{2.13}$$

2.2.3. *Asymptotic solution for the main beams around the critical lines L_1–L_5*

The similarity solution (2.5) and the reflection laws ((2.12) and (2.13)) are applied to build the asymptotic solutions around the critical lines L_1–L_5 for the two beams shown in figure 3. Taking the northward beam travelling from L_1 to L_5 as an example, the two ratios of sines of inclination angles at the points R_1 and R_2 shown in figure 3 take the forms

$$K_1 = \sqrt{1-\eta^2}/\eta, \quad K_2 = 1/K_1. \tag{2.14a,b}$$

The lengths of the critical lines L_1–L_5 in figure 3 take the values

$$d_1 = \sqrt{2}, \quad d_2 = \sqrt{2}\left(-1 + \frac{\sqrt{2-\eta^2}}{\eta}\right), \quad d_3 = 2\sqrt{2}, \quad d_4 = d_2, \quad d_5 = d_1, \tag{2.15a–e}$$

rescaled by the distance to the axis of the critical latitude in accordance with the non-dimensionalisation adopted by the asymptotic theory (Le Dizès & Le Bars 2017). The global coordinates (r, z) of a point P are transformed into the local coordinates $(x_{\parallel}, x_{\perp})$ for every critical line by computing the distances to the source S_c and to the corresponding critical line, respectively. The travelled distance $x_{\parallel}$ should be modified on the boundary according to (2.12a), and the amplitude C_0 should be modified on the boundary and axis according to (2.12b) and (2.13), respectively. We obtain for the northward beam the characteristics given in table 1. For the southward beam travelling from L_5 to L_1, the multiplicative inverses of the ratios (2.14) are taken, and the local coordinates and amplitudes for every critical line can be constructed similarly.

Up to this stage, we have described how to build the asymptotic solution along one complete revolution of the periodic orbit, from the critical latitude and back. However, it is natural to assume that the self-similar solution will continue propagating along the periodic characteristic path until its amplitude eventually becomes negligible. When the northward beam goes back to the critical latitude on the inner core, the outer part of the beam ($x_{\perp} > 0$) is expected to propagate forward for another cycle without being modified by the inner core. By contrast, the inner part ($x_{\perp} < 0$) is expected to reflect on the inner core and follow another path on L_6–L_8 before starting a new cycle. We shall see in § 2.2.4 that this different circuit has actually no impact on the beam: its new expression on L_1 is the same as if the inner core was not present. For this reason, the whole beam can be assumed to propagate forward for another cycle without considering the presence of the inner core. The same is naturally true for the southward beam. For each cycle, the self-similar nature

Critical line	$x_\parallel$	$x_\perp$	Amplitude
L_1	$\dfrac{z-r}{\sqrt{2}}$	$\dfrac{z+r-2}{\sqrt{2}}$	C_0
L_2	$d_1+\dfrac{z+r-2}{\sqrt{2}}$	$\dfrac{z-r-2}{\sqrt{2}}$	$\mathrm{i}C_0$
L_3	$(d_1+d_2)K_1^{-3}+\dfrac{r-z+2}{\sqrt{2}}$	$\dfrac{2\sqrt{2-\eta^2}/\eta-z-r}{\sqrt{2}}$	$\mathrm{i}C_0K_1^{-1/4}$
L_4	$d_1+d_2+d_3K_1^3+\dfrac{2\sqrt{2-\eta^2}/\eta-z-r}{\sqrt{2}}$	$\dfrac{r-z-2}{\sqrt{2}}$	$\mathrm{i}C_0$
L_5	$d_1+d_2+d_3K_1^3+d_4+\dfrac{z-r+2}{\sqrt{2}}$	$\dfrac{r+z-2}{\sqrt{2}}$	$\mathrm{i}C_0$

Table 1. Characteristics of the northward beam from L_1 to L_5.

of the local solution should be preserved since only C_0 and $x_\parallel$ are modified by reflections on the axis and boundaries. The asymptotic solution for the nth cycle can be expressed as

$$\sqrt{r}v_{\parallel n} = C_n H_m(x_{\parallel n}, \zeta_n). \tag{2.16}$$

The subscript n indicates a variable associated with the nth cycle. When $n = 0$, (2.16) is equivalent to (2.5) for the very first cycle. The variables of the subsequent cycles are related to those of the first $n = 0$ cycle by

$$x_{\parallel n} = x_{\parallel 0} + nL, \tag{2.17}$$

$$\zeta_n = \zeta_0 (x_{\parallel n}/x_{\parallel 0})^{1/3}, \tag{2.18}$$

$$C_n = C_0\, \mathrm{e}^{\mathrm{i}n\pi/2}, \tag{2.19}$$

where L is the travelled distance within one cycle, and $\pi/2$ is the phase shift induced by the reflection on the axis occurring once per cycle. Here, L takes the following formulas for different critical lines

$$L = d_1 + d_2 + d_3K_1^3 + d_4 + d_5, \quad \text{for} \quad L_1, L_2, L_4, L_5, \tag{2.20a}$$

$$L = (d_1 + d_2 + d_4 + d_5)K_1^{-3} + d_3, \quad \text{for} \quad L_3. \tag{2.20b}$$

Note that L does not change from one cycle to another and is the same for both beams. For the reflection $L_2 \leftrightarrow L_3$, L and $x_{\parallel 0}$ are discontinuous (see table 1 and (2.20a,b)), while $L/x_{\parallel 0}$ is continuous. The same is also true for the reflection $L_3 \leftrightarrow L_4$. Note also that the norm of the amplitude of the self-similar solution does not change after each cycle ($|C_n| = |C_0|$). This is associated with the symmetric character of each cycle, which guarantees that the phases of contraction and expansion experienced by the beam during one cycle exactly compensate.

The complete asymptotic solution associated with one beam is thus the sum of the solution (2.16) for every cycle. After $N + 1$ cycles, we obtain

$$\sqrt{r}v_\parallel^{(N)} = \sum_{n=0}^{N} C_n H_m(x_{\parallel n}, \zeta_n). \tag{2.21}$$

The self-similar solution decays with the travelled distance as $x_\parallel^{-5/12}$ (see (2.5) and (2.8)). This gives a behaviour in $n^{-5/12}$ of the coefficients of the series (2.21) that does not guarantee its absolute convergence. However, because C_n is oscillating with n (see (2.19)), the series does converge. The number of cycles can therefore be chosen as large as wanted. Using the relations ((2.17)–(2.19)), the series of the integrals (2.21) can be transformed to an integral of a geometric series

$$\sqrt{r}v_\parallel^{(N)} = C_0\left(\frac{x_{\parallel 0}}{2\sin\theta_c}\right)^{-m/3}\frac{\mathrm{e}^{-\mathrm{i}m\pi/2}}{(m-1)!}\int_0^\infty \mathrm{e}^{\mathrm{i}p\zeta_0-p^3}p^{m-1}\sum_{n=0}^{N}\mathrm{i}^n\,\mathrm{e}^{-np^3L/x_{\parallel 0}}\,\mathrm{d}p. \quad (2.22)$$

Moreover, with the closed form of the geometric series the solution can be expressed by two parts

$$\sqrt{r}v_\parallel^{(N)} = C_0G_m(x_{\parallel 0},x_\perp,L)+\varepsilon_m^{(N)}(x_{\parallel 0},x_\perp,L), \quad (2.23)$$

with

$$G_m(x_{\parallel 0},x_\perp,L) = \left(\frac{x_{\parallel 0}}{2\sin\theta_c}\right)^{-m/3} g_m(\zeta_0,L/x_{\parallel 0}), \quad (2.24a)$$

$$g_m(\zeta_0,L/x_{\parallel 0}) = \frac{\mathrm{e}^{-\mathrm{i}m\pi/2}}{(m-1)!}\int_0^\infty \frac{\mathrm{e}^{\mathrm{i}p\zeta_0-p^3}p^{m-1}}{1-\mathrm{i}\,\mathrm{e}^{-p^3L/x_{\parallel 0}}}\,\mathrm{d}p, \quad (2.24b)$$

and

$$\varepsilon_m^{(N)} = C_0\left(\frac{x_{\parallel 0}}{2\sin\theta_c}\right)^{-m/3}\frac{\mathrm{e}^{-\mathrm{i}m\pi/2}}{(m-1)!}\int_0^\infty \mathrm{e}^{\mathrm{i}p\zeta_0-p^3}p^{m-1}\frac{-\mathrm{i}^{N+1}\,\mathrm{e}^{-p^3L(N+1)/x_{\parallel 0}}}{1-\mathrm{i}\,\mathrm{e}^{-p^3L/x_{\parallel 0}}}\,\mathrm{d}p. \quad (2.25)$$

The correction term $\varepsilon_m^{(N)}$ behaves as

$$\varepsilon_m^{(N)} \sim -C_0\frac{\mathrm{e}^{-\mathrm{i}m\pi/2}}{(m-1)!}\frac{1}{3}\left(\frac{2\sin\theta_c}{L}\right)^{m/3}\frac{\Gamma(m/3)}{1-\mathrm{i}}\mathrm{i}^{N+1}N^{-m/3}, \quad (2.26)$$

as the number of cycles becomes large. It vanishes as the number of cycles tends to infinity. Therefore, in the limit $N\to\infty$, the asymptotic solution takes the form

$$\sqrt{r}v_\parallel = C_0G_m(x_\parallel,x_\perp,L). \quad (2.27)$$

Only the local coordinates in the very first cycle are needed to compute the asymptotic solution. Without any ambiguity, the subscript 0 denoting the very first cycle has been dropped for the parallel coordinate and similarity variable hereafter. The above discussion holds both for northward and southward rays. The final global asymptotic solution in the closed geometry is the sum of the solutions of both rays, that is

$$\sqrt{r}v_\parallel = C_0^{NW}G_m(x_\parallel^{NW},x_\perp^{NW},L)+C_0^{SW}G_m(x_\parallel^{SW},x_\perp^{SW},L), \quad (2.28)$$

where the superscripts NW and SW denote northward and southward rays, respectively. Equation (2.28) provides the description of the parallel velocity, while the azimuthal velocity v_ϕ can be derived from the phase relation (2.10).

2.2.4. *Asymptotic solution for the secondary beams around L_6 and L_8*

When the northward and southward beams come back to the critical latitude on the inner core, their corresponding critical lines become L_5 and L_1, respectively (see figure 6). Because these two critical lines are tangent to the surface, the part of the beams below L_5 and L_1 reflects on the inner boundary, while the other part goes straight. This particular reflection is referred to as diffraction by Baines (1971*b*) for a plane wave. The reflected beams are then along $L_6 \to L_7 \to L_8$ or $L_8 \to L_7 \to L_6$ for the northward or southward beams, respectively (see solid blue and green lines in figure 6). These reflected beams correspond to the two secondary weaker beams near the line $z = r$ observed in figure 1. In order to construct the corresponding asymptotic solution, curvature effects for the reflection on the inner core must be included. For this purpose, the non-penetrability condition is applied at the reflection point R (see figure 6) other than the critical one S_c, namely

$$\sin\theta^r v_\parallel^r \sim \sin\theta^i v_\parallel^i, \tag{2.29}$$

where θ^i and θ^r are incident and reflected inclination angles at the reflection point R, respectively. Note that their values are different from the critical values at the critical reflection point S_c due to the effect of curvature. The incident parallel velocity $v_\parallel^i$ is obtained by propagating the similarity solution from the critical latitude back to it along $L_1 \to L_2 \to L_3 \to L_4 \to L_5$ or the inverse sequence for the northward or southward beam, respectively, which is

$$v_\parallel^i = \frac{1}{\sqrt{r}} C_0 \mathrm{i} \frac{\mathrm{e}^{-\mathrm{i}m\pi/2}}{(m-1)!} \int_0^\infty \mathrm{e}^{\mathrm{i}px_\perp^i/E^{1/3}}\, \mathrm{e}^{-p^3 L/(2\sin\theta_c)} p^{m-1}\, \mathrm{d}p \tag{2.30}$$

in terms of the local coordinates $(x_\parallel^i, x_\perp^i)$. Note that $x_\parallel^i = L$ has been applied. Taking the northward beam as an example, according to the geometry shown in figure 6, $x_\perp^i$ and $x_\perp^r$ can be expressed as a function of θ^i as

$$x_\perp^i = \sqrt{2}\cos\theta^i - \sqrt{2}, \quad x_\perp^r = -\sqrt{2}\sin\theta^i. \tag{2.31a,b}$$

Note that the coordinates are also calculated with reference to the distance to the axis of the critical latitude by which the radius of the inner core is $\sqrt{2}$ (Le Dizès & Le Bars 2017). Moreover, $x_\perp^i$ can be expressed in terms of $x_\perp^r$ as

$$x_\perp^i = \sqrt{2 - (x_\perp^r)^2} - \sqrt{2}. \tag{2.32}$$

The variable $x_\perp^r$ being small within the beam, we obtain the following relation at the leading order:

$$x_\perp^i \sim \lambda (x_\perp^r)^2, \tag{2.33}$$

where $\lambda = \pm\sqrt{2}/4$. The minus and plus signs are for northward and southward beams, respectively. The inclination angles can also be expressed using $x_\perp^r$ as

$$\sin\theta^i = \left|\frac{x_\perp^r}{\sqrt{2}}\right|, \quad \sin\theta^r = \sqrt{1 - \left(\frac{x_\perp^r}{\sqrt{2}}\right)^2} \sim 1. \tag{2.34a,b}$$

Therefore, the parallel velocity of the reflected beam takes the following form:

$$v_\parallel^r \sim \left|\frac{x_\perp^r}{\sqrt{2}}\right| \frac{1}{\sqrt{r}} C_0 \mathrm{i} \frac{\mathrm{e}^{-\mathrm{i}m\pi/2}}{(m-1)!} \int_0^\infty \mathrm{e}^{\mathrm{i}p\lambda(x_\perp^r)^2/E^{1/3}}\, \mathrm{e}^{-p^3 L/(2\sin\theta_c)} p^{m-1}\, \mathrm{d}p. \tag{2.35}$$

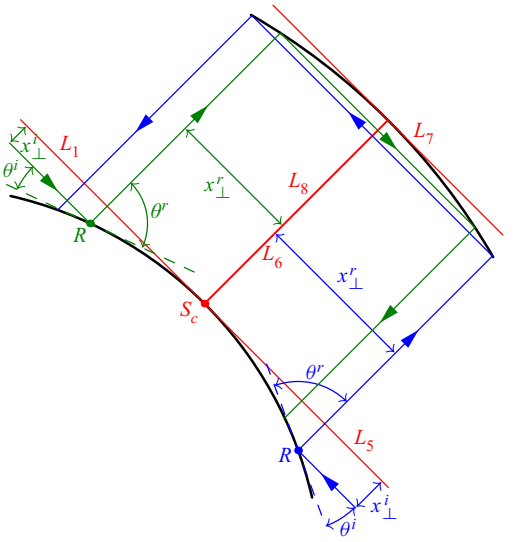

Figure 6. Schematic of the reflection on the inner boundary and the resulting rays around L_6–L_8. Blue and green lines are northward and southward rays; red lines are critical lines.

The phase is proportional to $(x^r_\perp)^2/E^{1/3}$, which means that $x^r_\perp$ scales with $E^{1/6}$. The reflected beam is therefore expected to be wider than the self-similar solution with a width of order $E^{1/6}$. Because of this larger transverse scale, it should not be affected by viscous diffusion within the shell. In other words, expression (2.35) for $v^r_\parallel$ is expected to remain valid on the whole segment L_6 (respectively L_8) for the northward beam (respectively for the southward beam). Each beam is then reflected twice on the outer boundary (see figure 6). Between these two reflection points on L_7, the beam recovers its initial width but because it travels a distance of order $E^{1/6}$, the viscous diffusion is still negligible. Moreover, the reflections on the outer boundary are perfectly symmetric, such that the northward and southward beams remain unchanged after these two reflections. The formula (2.35) then still holds for the northward or southward beam around L_8 or L_6, respectively. Namely, for each beam, the asymptotic solution (after rescaling with $1/\sqrt{r}$) is anti-symmetric about the centre line $z = r$.

Note that, contrary to the solution around the main beam L_1–L_5, the asymptotic solution (2.35) for L_6 and L_8 is no longer self-similar.

The asymptotic solution (2.35) corresponds to the first cycle only. The summation strategy used in the § 2.2.3 for L_1–L_5 can also be applied to construct the asymptotic solution around L_6 and L_8 after an infinite number of cycles. The parallel velocity for the n^{th} cycle is

$$v^{(n)}_\parallel \sim \left|\frac{x_\perp}{\sqrt{2}}\right| \frac{1}{\sqrt{r}} C_0 \mathrm{i}^n \frac{\mathrm{e}^{-\mathrm{i}m\pi/2}}{(m-1)!} \int_0^\infty \mathrm{e}^{\mathrm{i}p\lambda(x_\perp)^2/E^{1/3}}\, \mathrm{e}^{-p^3(nL)/(2\sin\theta_c)} p^{m-1}\, \mathrm{d}p, \qquad (2.36)$$

with the phase shift equal to i^n and the travelled distance equal to nL. The summation of the above formula from $n = 1$ to ∞ yields the asymptotic solution after an infinite number of cycles

$$v_\parallel \sim \left|\frac{x_\perp}{\sqrt{2}}\right| \frac{1}{\sqrt{r}} C_0 \frac{\mathrm{e}^{-\mathrm{i}m\pi/2}}{(m-1)!} \int_0^\infty \mathrm{e}^{\mathrm{i}p\lambda(x_\perp)^2/E^{1/3}} \frac{\mathrm{i}\,\mathrm{e}^{-p^3L/(2\sin\theta_c)}}{1-\mathrm{i}\,\mathrm{e}^{-p^3L/(2\sin\theta_c)}} p^{m-1}\, \mathrm{d}p. \qquad (2.37)$$

This formula holds for both northward and southward rays. The final solution is the sum of both solutions.

Finally, it is worth mentioning that, because $x_\perp$ is $O(E^{1/6})$ along L_6 and L_8 and C_0 is $O(E^{1/12})$, the amplitude of $v_\parallel$ is smaller than on the other lines and exhibits a new scaling in $E^{1/4}$.

2.3. *Numerical method*

In order to validate the asymptotic approach, we now consider the complete numerical solution of the linear viscous harmonic problem described in § 2.1. The governing equations (2.3) are solved numerically in spherical coordinates (ρ, ϑ, ϕ), where ρ, ϑ and ϕ are the radial distance from the centre of the sphere, polar and azimuthal angles, respectively. In order to compare the numerical results with asymptotic predictions obtained within a different cylindrical coordinate system, the azimuthal velocity is adopted since this velocity component is the same in both cylindrical and spherical frames.

As in Rieutord & Valdettaro (1997), the fields are expanded onto spherical harmonics in the polar and azimuthal directions and onto Chebyshev polynomials in the radial direction. We consider the expansion

$$\boldsymbol{v} = \sum_{l=0}^{+\infty} \sum_{m=-l}^{+l} u_m^l(\rho)\boldsymbol{R}_l^m + v_m^l(\rho)\boldsymbol{S}_l^m + w_m^l(\rho)\boldsymbol{T}_l^m, \tag{2.38}$$

with

$$\boldsymbol{R}_l^m = Y_l^m(\vartheta, \varphi)\boldsymbol{e}_\rho, \quad \boldsymbol{S}_l^m = \boldsymbol{\nabla} Y_l^m, \quad \boldsymbol{T}_l^m = \boldsymbol{\nabla} \times \boldsymbol{R}_l^m, \tag{2.39a–c}$$

where gradients are taken on the unit sphere. Projecting the curl of the momentum equation (2.3*a*) onto this basis yields (Rieutord 1987)

$$\left.\begin{aligned} E\Delta_l w^l + \mathrm{i}\omega w^l &= -A_l \rho^{l-1} \frac{\partial}{\partial \rho}\left(\frac{u^{l-1}}{\rho^{l-2}}\right) - A_{l+1}\rho^{-l-2}\frac{\partial}{\partial \rho}(\rho^{l+3}u^{l+1}), \\ E\Delta_l\Delta_l(\rho u^l) + \mathrm{i}\omega\Delta_l(\rho u^l) &= B_l \rho^{l-1} \frac{\partial}{\partial \rho}\left(\frac{w^{l-1}}{\rho^{l-1}}\right) + B_{l+1}\rho^{-l-2}\frac{\partial}{\partial \rho}(\rho^{l+2}w^{l+1}), \end{aligned}\right\}, \tag{2.40}$$

with

$$A_l = \frac{1}{l\sqrt{4l^2-1}}, \quad B_l = l^2(l^2-1)A_l, \quad \Delta_l = \frac{\mathrm{d}^2}{\mathrm{d}\rho^2} + \frac{2}{\rho}\frac{\mathrm{d}}{\mathrm{d}\rho} - \frac{l(l+1)}{\rho^2}. \tag{2.41a–c}$$

Axisymmetry ($m = 0$) is assumed. The unknown variables in (2.40) are only w^l and u^l. The third component v^l is related to u^l through the continuity equation (2.3*b*), that is

$$v^l = \frac{1}{\rho l(l+1)}\frac{\mathrm{d}\rho^2 u^l}{\mathrm{d}\rho}. \tag{2.42}$$

The no-slip boundary conditions on the outer core impose that

$$w^l = u^l = \frac{\mathrm{d}u^l}{\mathrm{d}\rho} = 0, \text{ at } \rho = 1. \tag{2.43}$$

The libration on the inner boundary imposes a forcing in the azimuthal direction. Its projection onto spherical harmonics yields the inhomogeneous boundary conditions on

the inner core

$$w^l = 2\sqrt{\frac{\pi}{3}}\eta\delta_{1,l}, \quad u^l = \frac{\mathrm{d}u^l}{\mathrm{d}\rho} = 0 \text{ at } \rho = \eta, \tag{2.44}$$

where $\delta_{i,j}$ is the Kronecker symbol.

Equations ((2.40)–(2.44)) are then discretised on the collocation points of the Gauss–Lobatto grid, which yields a linear system

$$\boldsymbol{A}\boldsymbol{x} = \boldsymbol{b}. \tag{2.45}$$

This linear algebraic system of equations is solved using the LU decomposition. The dimensions of the matrix $\boldsymbol{A}$ and the vector $\boldsymbol{b}$ depend on the spatial resolution which is related to the number of spherical harmonics (l_{max}) and the number of Chebyshev polynomials (N_r). For the computations at low Ekman numbers, large numbers of spherical harmonics and Chebyshev polynomials are necessary. Typically, in order to reach $E = 10^{-10}$, we use $l_{max} = 4000$ and $N_r = 2000$, which leads to a matrix size of 8004000. In that case, the memory footprint of the LU solver is approximately of 1.4 TB.

In order to display the wave structures and the scalings, the azimuthal velocity (v_ϕ) and viscous dissipation rate (D) are computed. The latter is defined as (Rieutord & Valdettaro 1997)

$$D = \frac{1}{2}E[S^2_{\rho\rho} + S^2_{\vartheta\vartheta} + S^2_{\phi\phi} + 2(S^2_{\rho\vartheta} + S^2_{\rho\phi} + S^2_{\vartheta\phi})], \tag{2.46}$$

where $\boldsymbol{S}$ is the rate-of-strain tensor. If the amplitudes of the velocities for the main (L_1–L_5) and secondary (L_6 and L_8) beams scale with $E^{1/12}$ and $E^{1/4}$, respectively, and the corresponding length scales are $E^{1/3}$ and $E^{1/6}$, the dissipation rates should scale with $E^{1/2}$ ($= E^{1+(1/12-1/3)\times 2}$) and $E^{7/6}$ ($= E^{1+(1/4-1/6)\times 2}$) respectively with the above definition. We validate these scalings numerically in the following.

3. Bulk solution

In this section, we compare the asymptotic and numerical solutions in the bulk region of the spherical shell for the two geometries $\eta = 0.35$ and $\sqrt{2}/2$, respectively. When deriving the similarity solutions ((2.5)–(2.10)), Le Dizès & Le Bars (2017) normalised lengths by the distance to the axis of the critical latitude, while lengths are non-dimensionalised by the radius of the outer shell in this paper. In order to adapt the theoretical results to our framework, the Ekman number defined by (2.1) is rescaled by $2/\eta^2$, and the coordinates rescaled by $\sqrt{2}/\eta$. The asymptotic solutions are obtained with the rescaled Ekman number and rescaled coordinates. In order to compare asymptotic and numerical solutions, the asymptotic solution has then to be divided by $\eta/\sqrt{2}$ or the numerical solutions multiplied by this quantity. The former is used when doing comparison in global coordinates, while the latter is used when doing comparison in local coordinates.

In the following, we shall only use the azimuthal component of the velocity for the comparisons. Other components of the velocity show similar behaviours, and will not be presented here.

3.1. *Aspect ratio* $\eta = 0.35$

The asymptotic solution for an infinite number of cycles is compared with the numerical one in figure 7. The inner and outer Ekman boundary layers and a region close to the axis are excluded since the asymptotic solution does not hold there. The asymptotic solution

is calculated using the expressions (2.28) and (2.37) for the corresponding critical lines L_1–L_5 and L_6 and L_8 within the following respective regions:

$$L_1 : \ \eta < z + r < 1 \quad \text{and} \quad z - r > 0; \tag{3.1a}$$

$$L_2 : \ \eta < z - r < 1; \tag{3.1b}$$

$$L_3 : \ 1 < z + r < \sqrt{2 - \eta^2}; \tag{3.1c}$$

$$L_4 : \ -1 < z - r < -\eta; \tag{3.1d}$$

$$L_5 : \ \eta < z + r < 1 \quad \text{and} \quad z - r < 0; \tag{3.1e}$$

$$L_6 : \ -\eta < z - r < 0; \tag{3.1f}$$

$$L_8 : \ 0 < z - r < \eta. \tag{3.1g}$$

These regions are chosen such that all the rays within them follow the same circuit. Note that we use a logarithmic colour scale over three decades in amplitude. This figure demonstrates that our asymptotic solution can qualitatively reproduce both global and local structures of the internal shear layer at the frequency $\omega^*/\Omega^* = \sqrt{2}$, especially as the Ekman number becomes small. The wave structure consists of an inclined rectangle and two beams near the centre line $z = r$. As the Ekman number decreases, the beams get thinner and their amplitude decreases, which is observed for both asymptotic and numerical solutions. The jumps of the asymptotic solution far away from the critical lines at high Ekman number occur at the endpoints of the calculation regions for every critical line (3.1) which tend to disappear as the Ekman number is reduced and the solution becomes more localised. These jumps may be smoothed by considering the rays outside the regions (3.1) which, however, follow a circuit different from $L_1 \leftrightarrow L_2 \leftrightarrow L_3 \leftrightarrow L_4 \leftrightarrow L_5$ and are therefore not considered here. In figure 7, S_{1-5} are the five sections crossing the main circuit, while S_6 and S_7 are crossing the two secondary beams near the centre line $z = r$. Quantitative comparisons will be made on these sections in the following.

Figure 8 compares the asymptotic velocity profiles for the northward and southward rays independently and their sum with the numerical profiles on three sections (S_2, S_3 and S_4) and at an Ekman number of $E = 10^{-10}$. The northward ray propagates from S_2 to S_4, while the southward one propagates from S_4 to S_2. Therefore, the amplitude of the northward ray decays from S_2 to S_4, while that of the southward ray decays from S_4 to S_2. The figure shows that only the superposition of both rays can approximate the numerical solution.

The asymptotic and numerical solutions at different Ekman numbers for the main beams on the section S_2 are compared in figure 9, which shows that our asymptotic solution performs better as the Ekman number decreases, as expected. At the lowest value of $E = 10^{-10}$, which starts to be relevant for geophysical applications, the agreement between the two solutions is remarkable, even far from the characteristic path. In figure 10, the same comparison is also made for the secondary beams on the sections S_6 and S_7. The numerical solutions on two different sections S_6 and S_7 are almost the same, which demonstrates the quasi-inviscid propagation of the beams along the critical lines L_6 and L_8. Better performance of asymptotic solutions with decreased Ekman number is also observed. Note that in figure 9 the narrower regions of the similarity variables at higher Ekman numbers are caused by the fixed length of the sections. The similarity variables on the sections take wider ranges of values for lower Ekman numbers (see (2.6)). The same is also true for the $x_\perp$ scaled with $E^{1/6}$ in figure 10.

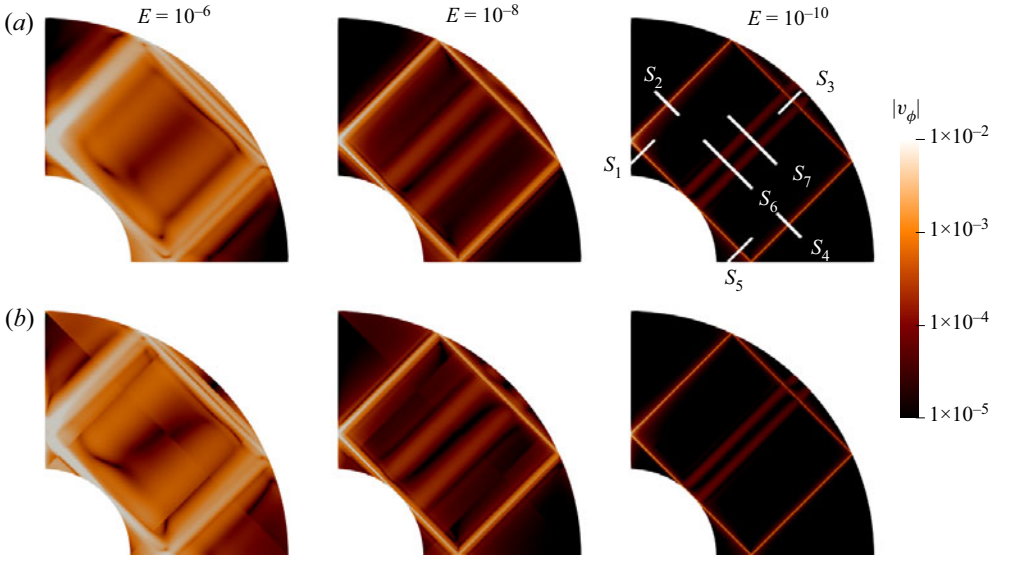

Figure 7. Contours of amplitudes of azimuthal velocity of numerical (*a*) and asymptotic (*b*) solutions for three Ekman numbers $E = 10^{-6}$, 10^{-8} and 10^{-10}.

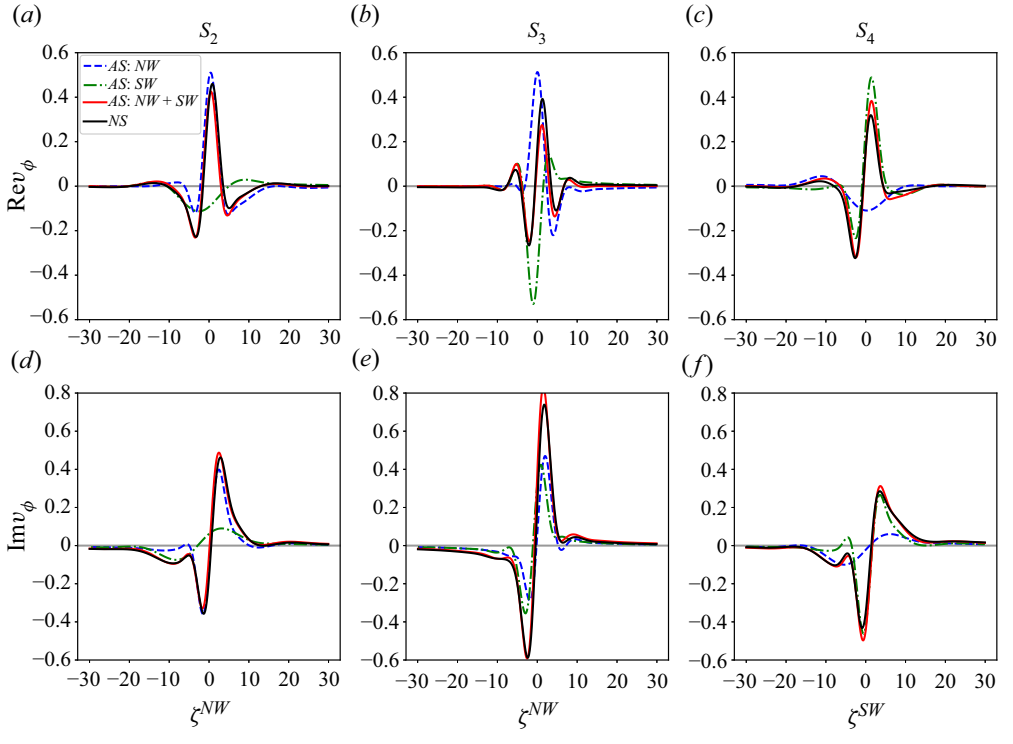

Figure 8. Azimuthal velocity profiles v_ϕ of the asymptotic solution (*AS*) for northward and southward rays and the sum of them and the numerical solution (*NS*) on three sections (S_2, S_3 and S_4, see figure 7) and at the Ekman number $E = 10^{-10}$.

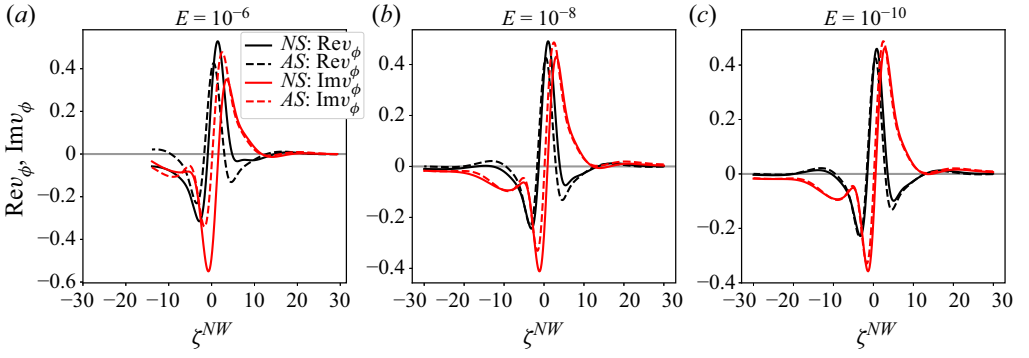

Figure 9. Azimuthal velocity profiles v_ϕ of the asymptotic and numerical solutions (*AS* and *NS*) at three Ekman numbers ($E = 10^{-6}$, 10^{-8} and 10^{-10}) for the main beams on the section S_2.

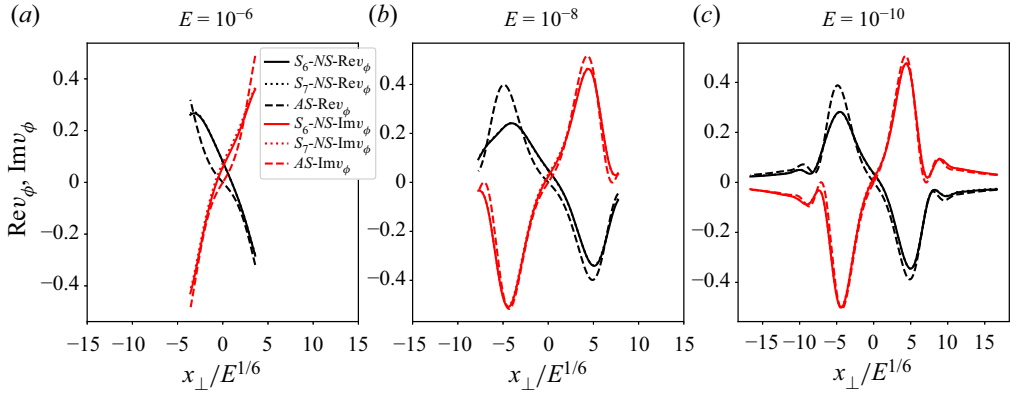

Figure 10. Same caption as above for the secondary beams on the sections S_6 and S_7.

The physical scalings of the numerical results in the range of Ekman number $10^{-10} \leq E \leq 10^{-6}$ are presented in figures 11 and 12 for the main and secondary beams, respectively. A fixed point at the intersection between the critical line L_2 and the section S_2 is selected to measure both velocity amplitude and dissipation rate at various Ekman numbers for the main beams. For the secondary beams, the same quantities are measured on the sections S_6 and S_7 in the narrow range $-5 \leqslant x_\perp/E^{1/6} \leqslant 5$ around the critical lines L_6 and L_8 since the quantities are close to zero on the critical lines. Both L^2 and L^∞ norms are considered for Ekman numbers ranging from 10^{-6} to 10^{-10}, as shown in figure 12. For the L^2 norm, results are scaled by the square root of the number of points into the region $-5 \leqslant x_\perp/E^{1/6} \leqslant 5$ since the number of points changes with the Ekman number. Figure 11(*a*) shows that the velocity amplitude of the main internal shear layer follows the scaling $E^{1/12}$ predicted by Le Dizès & Le Bars (2017) for an open geometry. This observation is to be contrasted with the scaling $E^{1/6}$ assumed by Kerswell (1995), who actually extrapolated the scaling of the shear layer emitted by an oscillating split disc to the one emitted by a librating inner core. The foregoing numerical results show that this simple extrapolation is not valid. We note that our results also further confirm the numerical observation made by Lin & Noir (2021) at comparatively higher Ekman numbers, where the scaling $E^{1/12}$ was favoured over $E^{1/6}$. For the secondary beams, figure 12(*a*) shows that the amplitude of the velocity also follows the predicted scaling $E^{1/4}$. Regarding the

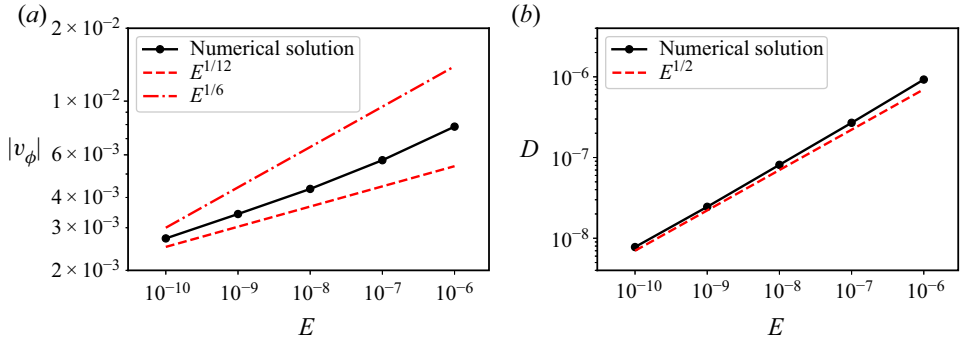

Figure 11. Scalings for the azimuthal velocity amplitude $|v_\phi|$ (a) and dissipation rate D (b) as a function of the Ekman number measured at the intersection between the section S_2 and the critical line L_2 (see figures 3 and 7).

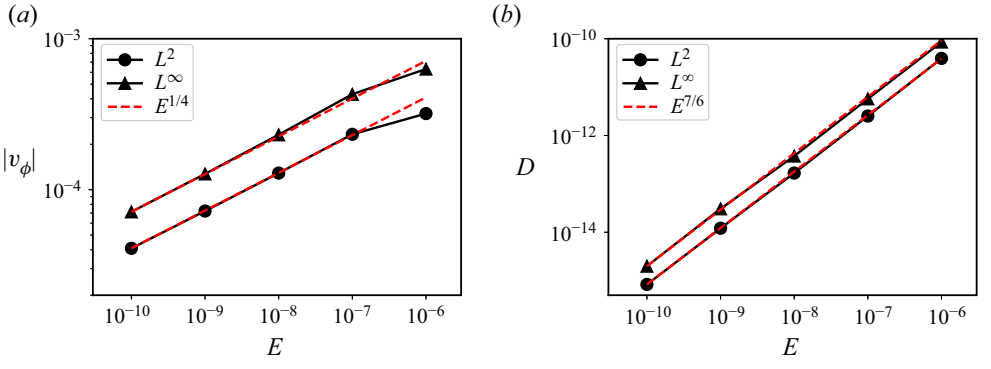

Figure 12. Same caption as in figure 11 but with quantities measured in the sections S_6 and S_7 around L_6/L_8 in the range $-5 \leqslant x_\perp/E^{1/6} \leqslant 5$.

dissipation rate, it follows the expected $E^{1/2}$ and $E^{7/6}$ scalings for the main and secondary beams, respectively. These scalings imply that the power dissipated by the respective beams vanishes as $E^{5/6}$ and $E^{4/3}$, which is weaker than the $E^{1/2}$ dissipation within the Ekman boundary layers. Libration in the whole shell is therefore mainly dissipated in the Ekman boundary layers.

Excluding the dissipation in the boundary layers by using stress-free boundary conditions, Rieutord & Valdettaro (2010) also found a vanishing dissipation as $E \to 0$ but with a lower power, namely as $E^{2/5}$ (see their figure 12). However, Rieutord & Valdettaro (2010) forced the oscillating flow with an $O(1)$ body force, while in the present case the forcing vanishes as $E \to 0$. This latter point underlines the importance of the nature of the forcing in the response of the fluid and the associated viscous dissipation.

The errors of the asymptotic solution relative to the numerical one are measured on the five sections S_{1-5} in the narrow range $-10 \leqslant \zeta \leqslant 10$ around the critical lines L_1–L_5 for the main beams. They are also computed on the two sections S_{6-7} in the narrow range $-5 \leqslant x_\perp/E^{1/6} \leqslant 5$ around the critical lines L_6 and L_8 for the secondary beams (see figures 3 and 7). The solution in these narrow regions is negligibly affected by the boundaries, the axis and the critical latitude where the asymptotic solution is not expected to perform well. The absolute error is measured by the norm of the difference between the theoretical predictions and numerical results averaged over the region of interest around the beam.

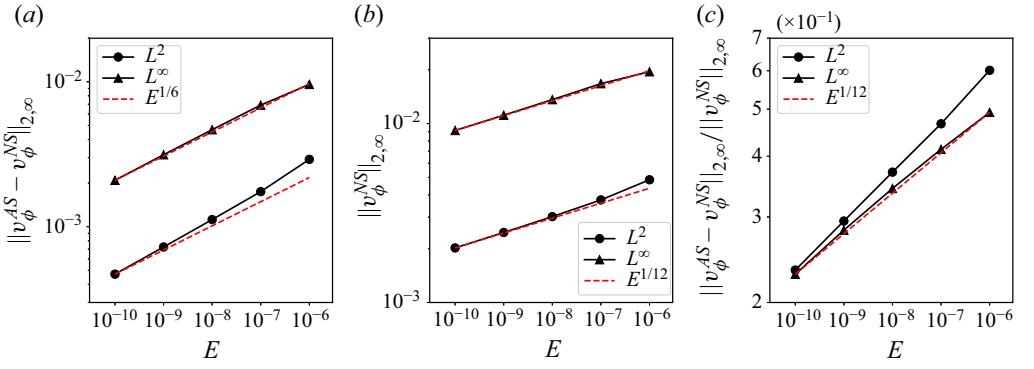

Figure 13. Absolute and relative errors on the azimuthal component of the velocity between the asymptotic and numerical solutions as a function of the Ekman number. The quantities are computed in the five sections S_{1-5} defined in figure 7 in the range of $-10 \leqslant \zeta \leqslant 10$.

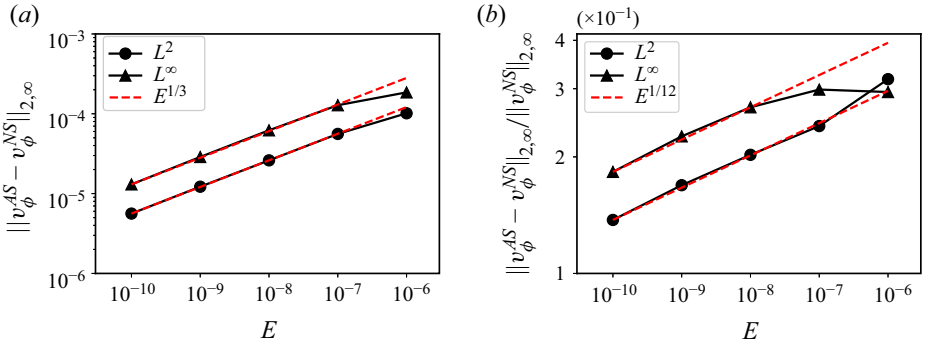

Figure 14. Same caption as in figure 13 but computed in the two sections S_{6-7} defined in figure 7 in the range of $-5 \leqslant x_\perp/E^{1/6} \leqslant 5$.

The relative error between the two approaches is obtained by normalising with the reference numerical solution. The absolute error plotted in figure 13(*a*) for the main beams is shown to scale with $E^{1/6}$ for both L^2 and L^∞ norms, while that for the secondary beams shown in figure 14(*a*) scales with $E^{1/3}$. Figure 13(*b*) demonstrates that the scaling in $E^{1/12}$ of the numerical solution for the main beams is very well predicted if we focus on the beam near the critical lines, similar to that for the secondary beams shown in figure 12(*a*). The relative errors for the main and secondary beams given in figures 13(*c*) and 14(*b*) follow the same scaling in $E^{1/12}$ as expected.

3.2. *Aspect ratio* $\eta = 1/\sqrt{2}$

We now consider the comparison between the theoretical asymptotic predictions and numerical results in a spherical shell with an aspect ratio of $\eta = 1/\sqrt{2}$. The reason behind this choice is the peculiar nature of the critical path, which connects the critical latitude to the pole and the equator without reflection on the boundaries. We use the same asymptotic approach as described previously.

Figure 15 compares the contours of the amplitude of the azimuthal velocity at $E = 10^{-10}$. Once again, our asymptotic solution can reproduce the beam structure, including the secondary weaker beam which corresponds to secondary reflections on the inner core

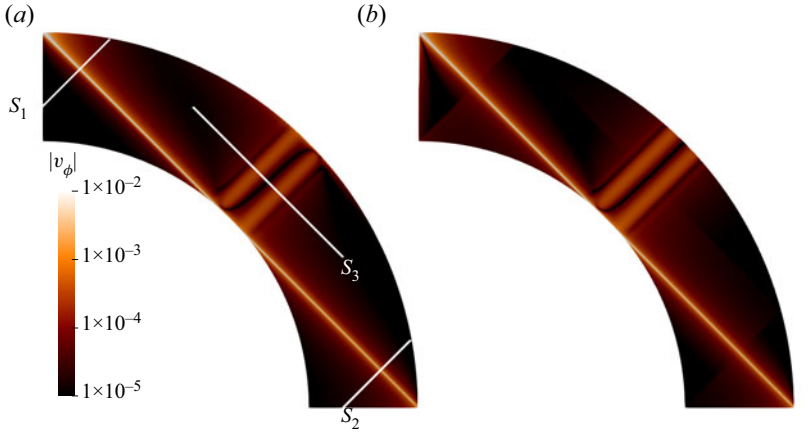

Figure 15. Contours of $|v_\phi|$ at $E = 10^{-10}$ and $\eta = 1/\sqrt{2}$ by numerical (a) and asymptotic (b) methods.

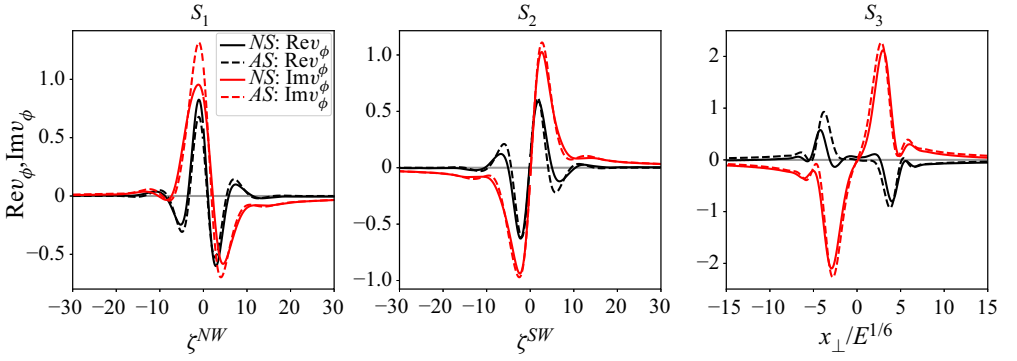

Figure 16. Velocity profiles along the three sections shown in figure 15 for $E = 10^{-10}$ and $\eta = 1/\sqrt{2}$.

close to the critical latitude. The velocity profiles are compared in figure 16 for the three sections defined in figure 15. We can see that a good agreement is obtained, even for this more pathological case involving reflections near the poles. The convergence properties as the Ekman number is reduced are the same as for the previous case $\eta = 0.35$.

4. Solution close to the axis

The self-similar solution (2.28) is singular on the axis due to the term $1/\sqrt{r}$. The region close to the axis has therefore been ignored in the asymptotic results discussed so far. Around the axis, the velocity and pressure can be expressed using Hankel transforms, as done by Le Dizès & Le Bars (2017) in an open geometry. In this section, we generalise this approach to the case of the spherical shell where the asymptotic solution now involves a series of rays propagating in opposite directions.

4.1. *Asymptotic theory*

We consider the reflections on the axis at the intersection of two adjacent critical lines L_1 and L_2 shown in figure 3 for the aspect ratio $\eta = 0.35$. In the spherical shell, two types of rays are involved there: the northward rays that reflect from L_1 to L_2, and the

southward ones that reflect from L_2 to L_1 after having performed two reflections on the outer sphere. Far away from the axis, the self-similar solution (2.28) holds. Close to the axis, the following Hankel transform for the velocity components and pressure can be used:

$$v_r = \int_0^\infty U_1(k)J_1(kr)\,\mathrm{e}^{\mathrm{i}\mu_1 z}\,\mathrm{d}k + \int_0^\infty U_2(k)J_1(kr)\,\mathrm{e}^{\mathrm{i}\mu_2 z}\,\mathrm{d}k, \tag{4.1a}$$

$$v_\phi = \int_0^\infty V_1(k)J_1(kr)\,\mathrm{e}^{\mathrm{i}\mu_1 z}\,\mathrm{d}k + \int_0^\infty V_2(k)J_1(kr)\,\mathrm{e}^{\mathrm{i}\mu_2 z}\,\mathrm{d}k, \tag{4.1b}$$

$$v_z = \int_0^\infty W_1(k)J_0(kr)\,\mathrm{e}^{\mathrm{i}\mu_1 z}\,\mathrm{d}k + \int_0^\infty W_2(k)J_0(kr)\,\mathrm{e}^{\mathrm{i}\mu_2 z}\,\mathrm{d}k, \tag{4.1c}$$

$$p = \int_0^\infty P_1(k)J_0(kr)\,\mathrm{e}^{\mathrm{i}\mu_1 z}\,\mathrm{d}k + \int_0^\infty P_2(k)J_0(kr)\,\mathrm{e}^{\mathrm{i}\mu_2 z}\,\mathrm{d}k, \tag{4.1d}$$

where $J_\alpha(\alpha = 0, 1)$ are the Bessel functions of the first kind and μ_1 and μ_2 are inviscid wavenumbers corresponding to the northward and southward rays, respectively. The four other viscous wavenumbers that could also be present in (4.1) (see Le Dizès 2015) have been omitted here because they are not present in the internal shear layer structure and not needed to smooth the singularity on the axis, as we shall see. Note also that, in an open geometry, only the component μ_1 associated with the northward ray is used (Le Dizès & Le Bars 2017), since the southward ray goes to infinity and never comes back close to the axis. At leading order, the two inviscid wavenumbers are related to k by

$$\mu_1 = k\frac{\cos\theta_c}{\sin\theta_c}, \quad \mu_2 = -k\frac{\cos\theta_c}{\sin\theta_c}. \tag{4.2a,b}$$

The corresponding amplitudes (U_1, V_1, W_1, P_1) and (U_2, V_2, W_2, P_2) are related to each other by the following expressions (Le Dizès 2015):

$$U_{1,2} = \mathrm{i}\cos\theta_c V_{1,2}, \tag{4.3a}$$

$$W_1 = -\sin\theta_c V_1, \tag{4.3b}$$

$$W_2 = \sin\theta_c V_2, \tag{4.3c}$$

$$kP_{1,2} = -2\sin\theta_c V_{1,2}. \tag{4.3d}$$

To describe the solution close to the reflection point on the axis, of coordinates $(0, \eta/\cos\theta_c)$, we introduce the local variables

$$\tilde{r} = r/E^{1/3}, \quad \tilde{z} = (z - \eta/\cos\theta_c)/E^{1/3}. \tag{4.4a,b}$$

The Hankel transform (4.1) can then be written as

$$v_r = \mathrm{i}\cos\theta_c\left[\int_0^\infty \tilde{V}_1 J_1(\tilde{k}\tilde{r})\,\mathrm{e}^{\mathrm{i}\tilde{k}\gamma\tilde{z}}\,\mathrm{d}\tilde{k} + \int_0^\infty \tilde{V}_2 J_1(\tilde{k}\tilde{r})\,\mathrm{e}^{-\mathrm{i}\tilde{k}\gamma\tilde{z}}\,\mathrm{d}\tilde{k}\right], \tag{4.5a}$$

$$v_\phi = \int_0^\infty \tilde{V}_1 J_1(\tilde{k}\tilde{r})\,\mathrm{e}^{\mathrm{i}\tilde{k}\gamma\tilde{z}}\,\mathrm{d}\tilde{k} + \int_0^\infty \tilde{V}_2 J_1(\tilde{k}\tilde{r})\,\mathrm{e}^{-\mathrm{i}\tilde{k}\gamma\tilde{z}}\,\mathrm{d}\tilde{k}, \tag{4.5b}$$

$$v_z = \sin\theta_c\left[-\int_0^\infty \tilde{V}_1 J_0(\tilde{k}\tilde{r})\,\mathrm{e}^{\mathrm{i}\tilde{k}\gamma\tilde{z}}\,\mathrm{d}\tilde{k} + \int_0^\infty \tilde{V}_2 J_0(\tilde{k}\tilde{r})\,\mathrm{e}^{-\mathrm{i}\tilde{k}\gamma\tilde{z}}\,\mathrm{d}\tilde{k}\right], \tag{4.5c}$$

$$p = -2\sin\theta_c E^{1/3}\left[\int_0^\infty \tilde{V}_1\frac{J_0(\tilde{k}\tilde{r})}{\tilde{k}}\,\mathrm{e}^{\mathrm{i}\tilde{k}\gamma\tilde{z}}\,\mathrm{d}\tilde{k} + \int_0^\infty \tilde{V}_2\frac{J_0(\tilde{k}\tilde{r})}{\tilde{k}}\,\mathrm{e}^{-\mathrm{i}\tilde{k}\gamma\tilde{z}}\,\mathrm{d}\tilde{k}\right], \tag{4.5d}$$

with $\gamma = 1/\tan\theta_c$.

Expressions for $\tilde{V}_1$ and $\tilde{V}_2$ are sought by matching the solution close to the axis (4.5) with the self-similar solution in the bulk ((2.28) and (2.10)). When both $\tilde{r}$ and $\tilde{z}$ go to infinity, the limit of v_ϕ (4.5*b*) is

$$v_\phi \sim \frac{1}{\sqrt{2\pi\tilde{r}}}\int_0^\infty \frac{\tilde{V}_1(\tilde{k})}{\sqrt{\tilde{k}}}\,\mathrm{e}^{\mathrm{i}\tilde{k}(\tilde{r}+\gamma\tilde{z})-\mathrm{i}3\pi/4}\,\mathrm{d}\tilde{k} \tag{4.6a}$$

$$+\frac{1}{\sqrt{2\pi\tilde{r}}}\int_0^\infty \frac{\tilde{V}_1(\tilde{k})}{\sqrt{\tilde{k}}}\,\mathrm{e}^{\mathrm{i}\tilde{k}(-\tilde{r}+\gamma\tilde{z})+\mathrm{i}3\pi/4}\,\mathrm{d}\tilde{k} \tag{4.6b}$$

$$+\frac{1}{\sqrt{2\pi\tilde{r}}}\int_0^\infty \frac{\tilde{V}_2(\tilde{k})}{\sqrt{\tilde{k}}}\,\mathrm{e}^{\mathrm{i}\tilde{k}(\tilde{r}-\gamma\tilde{z})-\mathrm{i}3\pi/4}\,\mathrm{d}\tilde{k} \tag{4.6c}$$

$$+\frac{1}{\sqrt{2\pi\tilde{r}}}\int_0^\infty \frac{\tilde{V}_2(\tilde{k})}{\sqrt{\tilde{k}}}\,\mathrm{e}^{\mathrm{i}\tilde{k}(-\tilde{r}-\gamma\tilde{z})+\mathrm{i}3\pi/4}\,\mathrm{d}\tilde{k}, \tag{4.6d}$$

using the asymptotic behaviour of the Bessel function at infinity. The four components correspond to the incident northward rays (L_1), the reflected northward rays (L_2), the incident southward rays (L_2) and the reflected southward rays (L_1). The former two components for the incident and reflected northward rays imply that there is a phase shift from the incident to reflected rays, which is $3\pi/2$ for the azimuthal velocity. Considering the phase (2.10) between $v_\parallel$ and v_ϕ, the phase shift for $v_\parallel$ is $\pi/2$. The same is true for the southward rays.

On the other hand, the self-similar solution ((2.28) and (2.10)) for v_ϕ in the bulk takes the following form close to the intersection point on the axis ($r \to 0, z \to \eta/\cos\theta_c$):

$$v_\phi \sim \mathrm{i}\frac{1}{\sqrt{r}}C_0^{NW}G_m(L_{NW}, \sin\theta_c(\tilde{r}+\gamma\tilde{z}), L) \tag{4.7a}$$

$$+\frac{1}{\sqrt{r}}C_0^{NW}G_m(L_{NW}, \sin\theta_c(-\tilde{r}+\gamma\tilde{z}), L) \tag{4.7b}$$

$$+\mathrm{i}\frac{1}{\sqrt{r}}C_0^{SW}G_m(L_{SW}, \sin\theta_c(\tilde{r}-\gamma\tilde{z}), L) \tag{4.7c}$$

$$+\frac{1}{\sqrt{r}}C_0^{SW}G_m(L_{SW}, \sin\theta_c(-\tilde{r}-\gamma\tilde{z}), L), \tag{4.7d}$$

where L_{NW} and L_{SW} are the travelled distances of the northward and southward rays from the source to the intersection point on the axis, respectively. Here, L is the travelled distance within one cycle (2.20).

By matching (4.6) with (4.7), the amplitudes $\tilde{V}_1$ and $\tilde{V}_2$ are obtained as follows:

$$\tilde{V}_1 = E^{-1/6}C_0^{NW}\sqrt{2\pi}\frac{\tilde{k}^{m-1/2}}{\sin^m\theta_c}\,\mathrm{e}^{\mathrm{i}5\pi/4}\frac{\mathrm{e}^{-\mathrm{i}m\pi/2}}{(m-1)!}\frac{\mathrm{e}^{-L_{NW}\tilde{k}^3/(2\sin^4\theta_c)}}{1-\mathrm{i}\,\mathrm{e}^{-L\tilde{k}^3/(2\sin^4\theta_c)}}, \tag{4.8a}$$

$$\tilde{V}_2 = E^{-1/6}C_0^{SW}\sqrt{2\pi}\frac{\tilde{k}^{m-1/2}}{\sin^m\theta_c}\,\mathrm{e}^{\mathrm{i}5\pi/4}\frac{\mathrm{e}^{-\mathrm{i}m\pi/2}}{(m-1)!}\frac{\mathrm{e}^{-L_{SW}\tilde{k}^3/(2\sin^4\theta_c)}}{1-\mathrm{i}\,\mathrm{e}^{-L\tilde{k}^3/(2\sin^4\theta_c)}}. \tag{4.8b}$$

It is worth pointing out the factor $E^{-1/6}$ in front of the ray amplitudes C_0^{NW} and C_0^{SW}. These amplitudes are $O(E^{1/12})$, which means that $\tilde{V}_1$ and $\tilde{V}_2$ scale as $E^{-1/12}$. This implies

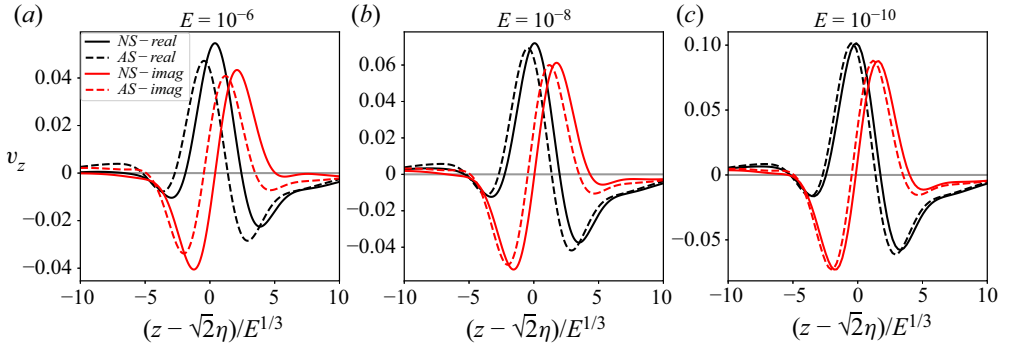

Figure 17. Comparison of asymptotic solutions and numerical results of v_z on the axis for three Ekman numbers.

that the solution close to the reflection point is expected to grow infinitely as E goes to zero. It clearly shows the singular nature of the small Ekman number limit for this problem: the linear solution is expected to vanish everywhere except in the boundary layer on the inner sphere (where it is finite) and at this single reflection point on the axis (where it diverges).

4.2. *Comparison with numerical results*

The asymptotic solution close to the axis (4.5) with the amplitudes (4.8) is compared with the numerical results. Figure 17 compares the asymptotic and numerical solutions along the rotation axis for three Ekman numbers. Only the velocity component v_z is concerned, as the other two components are zero by axisymmetry. We obtain a good agreement between the theoretical predictions and the numerical results. As the Ekman number decreases, our asymptotic solution converges to the numerical one. Figure 18 shows the same comparison but on the line perpendicular to the rotation axis and passing by the reflection point $(0, \eta/\cos\theta_c)$. All three velocity components are considered. Contrary to previous results, only one part of the asymptotic solution (namely the imaginary part of v_r and the real part of v_z and v_ϕ) performs well. However, as we decrease the Ekman number, the other part of the asymptotic solution approaches the corresponding numerical one, although there are still obvious differences for our lowest Ekman number 10^{-10}. Interestingly, the absolute errors of the asymptotic solution close to axis are found to be almost invariant with the Ekman number (not shown here), while the relative errors scale with $E^{1/12}$ similarly to those in the bulk (see figures 13*c* and 14*b*). This suggests that both the errors of the asymptotic solutions close to axis and in the bulk come from the same source, which could be a weaker singularity at the critical latitude. It is suspected that the order of this singularity is $O(E^{1/6})$, which corresponds to $m = 1$ if its solution is still self-similar. Its contribution to the asymptotic solution is not considered here, since we are concerned with the leading-order response, but could be further investigated in future studies.

5. Conclusion

Using both numerical and asymptotic methods, we have studied the harmonic response that is generated in a rotating spherical shell by librating the inner sphere at the frequency $\omega = \sqrt{2}\Omega$ where Ω is the angular frequency of the fluid. For this particular frequency, the inertial waves propagate along rays inclined at 45 degrees with respect to the equatorial

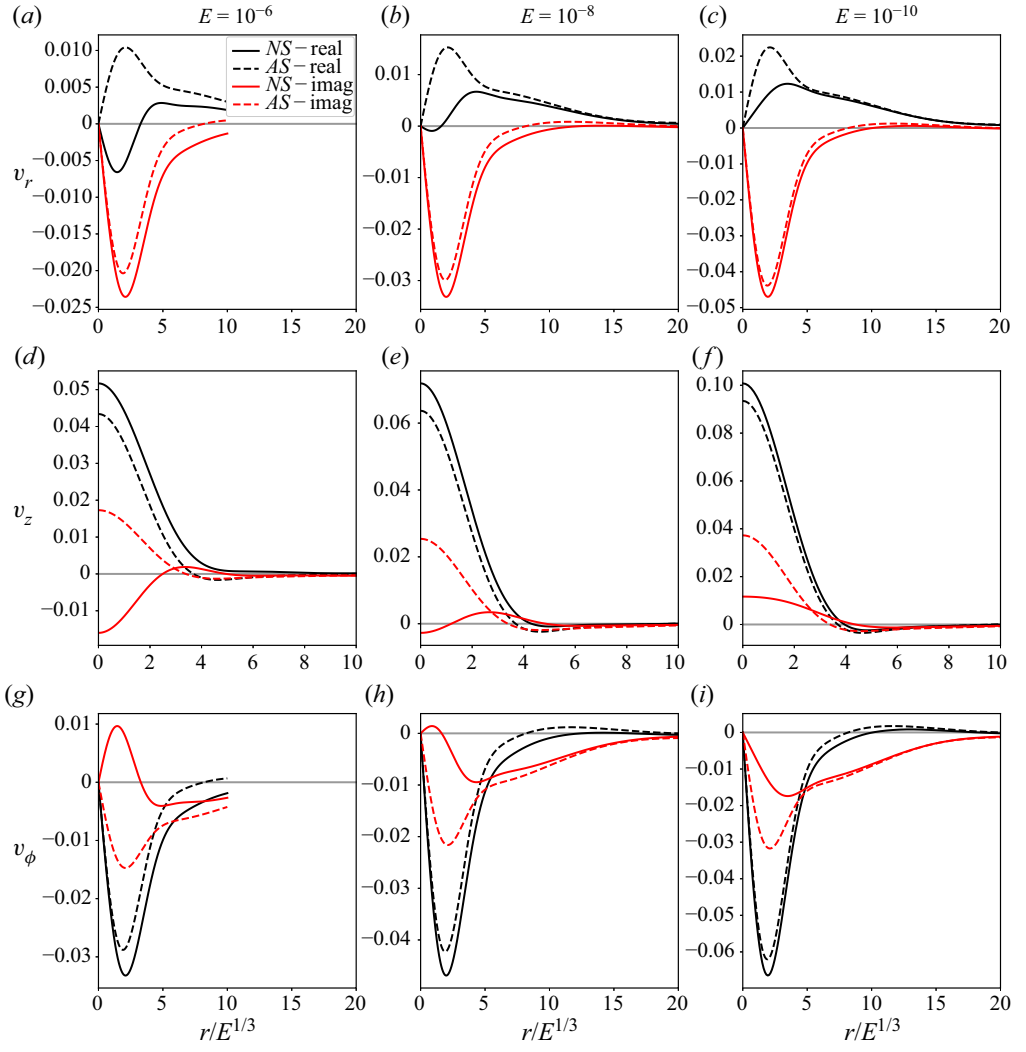

Figure 18. Comparison of asymptotic solutions and numerical results of three velocity components on the line perpendicular to the axis at the reflection point $(0, \eta/\cos\theta_c)$ for three Ekman numbers.

plane and therefore form closed periodic orbits in a spherical shell. We have shown, by considering numerical results down to Ekman numbers $E = 10^{-10}$, that the harmonic response is mainly governed by the internal shear layers that are emitted from the critical latitude of the inner sphere. In Le Dizès & Le Bars (2017), it was shown that these internal shear layers are concentrated wave beams that can be described in an open geometry and at small Ekman numbers by the similarity solution initially introduced by Moore & Saffman (1969). Here, we have further generalised this model and constructed an asymptotic solution by monitoring the reflections of the critical-latitude beams on the boundaries and on the axis. Despite the curvature of the boundaries, owing to the large-wavenumber approximation (Baines 1971*a*), the reflection laws on a locally planar boundary (Le Dizès 2020) can be applied to construct the self-similar form of the main $E^{1/3}$ shear layers. The diffraction (Baines 1971*b*) on the inner boundary creates a secondary $E^{1/6}$ shear layer

whose asymptotic form is not self-similar. The two asymptotic forms give the scalings of the velocity amplitudes in $E^{1/12}$ and $E^{1/4}$ for the main and secondary shear layers, respectively. The respective local dissipation rates are predicted to scale with $E^{1/2}$ and $E^{7/6}$. We have finally obtained that the asymptotic solution can be written as an infinite sum of similarity solutions for the main shear layers. Interestingly, this sum converges owing to the phase shift of $\pi/2$ that the beams experience at each reflection on the rotation axis. The same summation strategy can also be applied for the non-self-similar form of the secondary shear layers and a convergent sum is thus obtained for the same reason.

The asymptotic solution has been compared with the numerical solution of the linearised equations for several Ekman numbers and two values of the shell aspect ratio, and a very good agreement has been demonstrated. The relative error has been shown to be of order $E^{1/12}$. We suspect that it could be associated with a weaker singularity at the critical latitude. An immediate consequence of our result is the scaling in $E^{1/12}$ of the harmonic response velocity, as predicted for the internal shear layer amplitude in an open geometry (Le Dizès & Le Bars 2017). This scaling was also observed in recent simulations by Lin & Noir (2021) but it contrasts with the $E^{1/6}$ scaling previously reported in the literature in similar contexts (Kerswell 1995; Calkins *et al.* 2010; Favier *et al.* 2014; Cébron *et al.* 2019).

We have also analysed the solution close to the point on the rotation axis where the critical-latitude beam reflects. The similarity solution diverges at this point. We have provided a new asymptotic expression describing the solution in the $O(E^{1/3})$ neighbourhood of this point. We have in particular shown that the solution also scales as $E^{-1/12}$ in this region.

It is worth emphasising that the theoretical method that has been used to build the asymptotic solution can be applied to other situations. For instance, one can imagine considering other libration frequencies. As long as $\omega < 2\Omega$, critical-latitude beams are expected to be excited. These beams would propagate in the spherical shell, be reflected on boundaries and form a complex ray pattern depending on the aspect ratio and the frequency. If the critical-latitude beams converge towards an attractor, or if they travel along a periodic orbit, as in the present case, the solution is expected to be localised along these beams. The solution could then be obtained as a sum of similarity solutions. Because these similarity solutions decrease slowly along their direction of propagation as $x_{\|}^{-5/12}$, the convergence of this sum would depend on the phase shift that the beam experiences on the periodic orbit or on the attractor, that is on the number of reflections on the axis. If the sum converges, we claim that our approach should apply. The other situation where the sum does not converge is naturally of interest. We suspect that in that case one obtains a completely different response with a new scaling in E, and probably multi-layer structures as observed in the Stewartson layers between differentially rotating spheres (Stewartson 1966).

Finally, it is important to mention that we have limited our analysis to libration to be able to use an existing model for the structure of the critical-latitude beam. Yet, critical-latitude beams exist for other types of harmonic forcing. One similar viscous forcing is the precession of a spherical shell for which the critical-latitude beams are inclined at 30° with respect to the rotation axis and form a periodic orbit if the inner core radius is smaller than half the outer one (Hollerbach & Kerswell 1995). The asymptotic solution obtained in the present paper for libration is expected to work similarly in that case with the same singularity strength ($m = 5/4$) for the critical latitude beam. The modification associated with the azimuthal dependence of precession is indeed expected to just add a phase factor to the solution.

Another stronger forcing is the periodic translation of a sphere generating the famous Saint Andrews cross pattern (Mowbray & Rarity 1967; Greenspan 1968) which is nothing but the pattern left by the critical-latitude beams. If these beams can be described by the similarity solution of Moore & Saffman (1969), a similar approach could then naturally be developed in those cases and further generalised to closed geometries.

Acknowledgements. Centre de Calcul Intensif d'Aix-Marseille is acknowledged for granting access to its high performance computing resources. The authors are grateful to an anonymous reviewer for a decisive comment concerning curvature effects and the weaker central beam which drastically improved the paper.

Funding. J.H. acknowledges China Scholarship Council for financial support (CSC 202008440260).

Declaration of interests. The authors report no conflict of interest.

Author ORCIDs.
Jiyang He https://orcid.org/0000-0003-4176-1829;
Benjamin Favier https://orcid.org/0000-0002-1184-2989;
Michel Rieutord https://orcid.org/0000-0002-9395-6954;
Stéphane Le Dizès https://orcid.org/0000-0001-6540-0433.

Appendix A. Justification of the absence of back-reflected beams

In this section, our objective is to show that no back-reflected beams are present when the beam described by the similarity solution reflects on a curved boundary. This result is obtained by proving that this beam is composed of wavelengths which are small compared with the radius of curvature of the boundary. For this purpose, one just has to notice that the similarity solution ((2.5)–(2.7)) is given by an integral of the form

$$I = \int_0^\infty \mathrm{e}^{\mathrm{i}p(x_\perp/E^{1/3})}\,\mathrm{e}^{-p^3(x_\parallel/2\sin\theta_c)} p^{m-1}\,\mathrm{d}p, \tag{A1}$$

and that, since this integral converges for any $m > 0$ and $x_\parallel > 0$, we can replace the boundaries 0 and ∞ of the integral by ε and $1/\varepsilon$ for any $\varepsilon \to 0$. Thus, after a change of integration variable we obtain

$$I \sim E^{m/3} \int_{\varepsilon/E^{1/3}}^{(1/\varepsilon)/E^{1/3}} \mathrm{e}^{\mathrm{i}\tilde{p}x_\perp}\,\mathrm{e}^{-E\tilde{p}^3(x_\parallel/2\sin\theta_c)} \tilde{p}^{m-1}\,\mathrm{d}\tilde{p}. \tag{A2}$$

The first term $\mathrm{e}^{\mathrm{i}\tilde{p}x_\perp}$ of the integrand denotes the carrier with $\tilde{p}$ as the wavenumber, while the rest can be considered as the amplitude. If we choose $\varepsilon = E^{1/6}$, the wavenumbers fall into the following interval:

$$E^{-1/6} < \tilde{p} < E^{-1/2}, \tag{A3}$$

which means that the wavenumbers are large in the small Ekman number limit. In other words, the wavelengths governing the similarity solution are small compared with the $O(1)$ scale of the boundary. As explained in Baines (1971*a*), this guarantees that the reflection of the beam on the boundary is as if the boundary was locally flat. No back-reflected beams are therefore created.

References

Aldridge, K.D. & Toomre, A. 1969 Axisymmetric inertial oscillations of a fluid in a rotating spherical container. *J. Fluid Mech.* **37** (2), 307–323.

BAINES, P.G. 1971*a* The reflexion of internal/inertial waves from bumpy surfaces. *J. Fluid Mech.* **46** (2), 273–291.

BAINES, P.G. 1971*b* The reflexion of internal/inertial waves from bumpy surfaces. Part 2. Split reflexion and diffraction. *J. Fluid Mech.* **49** (1), 113–131.

BROUZET, C., ERMANYUK, E.V., JOUBAUD, S., SIBGATULLIN, I. & DAUXOIS, T. 2016 Energy cascade in internal-wave attractors. *Europhys. Lett.* **113** (4), 44001.

CALKINS, M.A., NOIR, J., ELDREDGE, J.D. & AURNOU, J.M. 2010 Axisymmetric simulations of libration-driven fluid dynamics in a spherical shell geometry. *Phys. Fluids* **22** (8), 086602.

CÉBRON, D., LAGUERRE, R., NOIR, J. & SCHAEFFER, N. 2019 Precessing spherical shells: flows, dissipation, dynamo and the lunar core. *Geophys. J. Intl* **219** (Supplement_1), S34–S57.

CÉBRON, D., LE BARS, M., NOIR, J. & AURNOU, J.M. 2012 Libration driven elliptical instability. *Phys. Fluids* **24** (6), 061703.

DAUXOIS, T., JOUBAUD, S., ODIER, P. & VENAILLE, A. 2018 Instabilities of internal gravity wave beams. *Annu. Rev. Fluid Mech.* **50**, 131–156.

FAVIER, B., BARKER, A.J., BARUTEAU, C. & OGILVIE, G.I. 2014 Non-linear evolution of tidally forced inertial waves in rotating fluid bodies. *Mon. Not. R. Astron. Soc.* **439** (1), 845–860.

FAVIER, B., GRANNAN, A.M., LE BARS, M. & AURNOU, J.M. 2015 Generation and maintenance of bulk turbulence by libration-driven elliptical instability. *Phys. Fluids* **27** (6), 066601.

GRANNAN, A.M., LE BARS, M., CÉBRON, D. & AURNOU, J.M. 2014 Experimental study of global-scale turbulence in a librating ellipsoid. *Phys. Fluids* **26** (12), 126601.

GREENSPAN, H.P. 1968 *The Theory of Rotating Fluids*. CUP Archive.

HOLLERBACH, R. & KERSWELL, R.R. 1995 Oscillatory internal shear layers in rotating and precessing flows. *J. Fluid Mech.* **298**, 327–339.

KERSWELL, R.R. 1995 On the internal shear layers spawned by the critical regions in oscillatory Ekman boundary layers. *J. Fluid Mech.* **298**, 311–325.

KISTOVICH, Y.V. & CHASHECHKIN, Y.D. 1994 Reflection of packets of internal waves from a rigid plane in a viscous fluid. *Izv. Atmos. Ocean. Phys.* **30**, 752–758.

KOCH, S., HARLANDER, U., EGBERS, C. & HOLLERBACH, R. 2013 Inertial waves in a spherical shell induced by librations of the inner sphere: experimental and numerical results. *Fluid Dyn. Res.* **45** (3), 035504.

LE BARS, M., CÉBRON, D. & LE GAL, P. 2015 Flows driven by libration, precession, and tides. *Annu. Rev. Fluid Mech.* **47** (1), 163–193.

LE DIZÈS, S. 2015 Wave field and zonal flow of a librating disk. *J. Fluid Mech.* **782**, 178–208.

LE DIZÈS, S. 2020 Reflection of oscillating internal shear layers: nonlinear corrections. *J. Fluid Mech.* **899**, A21.

LE DIZÈS, S. & LE BARS, M. 2017 Internal shear layers from librating objects. *J. Fluid Mech.* **826**, 653–675.

LE REUN, T., FAVIER, B. & LE BARS, M. 2019 Experimental study of the nonlinear saturation of the elliptical instability: inertial wave turbulence versus geostrophic turbulence. *J. Fluid Mech.* **879**, 296–326.

LEMASQUERIER, D., GRANNAN, A.M., VIDAL, J., CÉBRON, D., FAVIER, B., BARS, M.L. & AURNOU, J.M. 2017 Libration-driven flows in ellipsoidal shells. *J. Geophys. Res. Planets* **122** (9), 1926–1950.

LIN, Y. & NOIR, J. 2021 Libration-driven inertial waves and mean zonal flows in spherical shells. *Geophys. Astrophys. Fluid Dyn.* **115** (3), 258–279.

LIN, Y. & OGILVIE, G.I. 2018 Tidal dissipation in rotating fluid bodies: the presence of a magnetic field. *Mon. Not. R. Astron. Soc.* **474** (2), 1644–1656.

LIN, Y. & OGILVIE, G.I. 2021 Resonant tidal responses in rotating fluid bodies: global modes hidden beneath localized wave beams. *Astrophys. J. Lett.* **918** (1), L21.

MAAS, L.R.M. 2001 Wave focusing and ensuing mean flow due to symmetry breaking in rotating fluids. *J. Fluid Mech.* **437**, 13–28.

MAAS, L., BENIELLI, D., SOMMERIA, J. & LAM, F.-P. 1997 Observation of an internal wave attractor in a confined, stably stratified fluid. *Nature* **388** (6642), 557–561.

MANDERS, A.M.M. & MAAS, L.R.M. 2003 Observations of inertial waves in a rectangular basin with one sloping boundary. *J. Fluid Mech.* **493**, 59–88.

MCEWAN, A.D. 1970 Inertial oscillations in a rotating fluid cylinder. *J. Fluid Mech.* **40** (3), 603–640.

MOORE, D.W. & SAFFMAN, P.G. 1969 The structure of free vertical shear layers in a rotating fluid and the motion produced by a slowly rising body. *Phil. Trans. R. Soc. Lond.* A **264** (1156), 597–634.

MORIZE, C., LE BARS, M., LE GAL, P. & TILGNER, A. 2010 Experimental determination of zonal winds driven by tides. *Phys. Rev. Lett.* **104** (21), 214501.

MOWBRAY, D.E. & RARITY, B.S.H. 1967 A theoretical and experimental investigation of the phase configuration of internal waves of small amplitude in a density stratified liquid. *J. Fluid Mech.* **28**, 1–16.

NOIR, J., BRITO, D., ALDRIDGE, K. & CARDIN, P. 2001 Experimental evidence of inertial waves in a precessing spheroidal cavity. *Geophys. Res. Lett.* **28** (19), 3785–3788.

NOIR, J., CÉBRON, D., LE BARS, M., SAURET, A. & AURNOU, J.M. 2012 Experimental study of libration-driven zonal flows in non-axisymmetric containers. *Phys. Earth Planet. Inter.* **204**, 1–10.

NOIR, J., HEMMERLIN, F., WICHT, J., BACA, S.M. & AURNOU, J.M. 2009 An experimental and numerical study of librationally driven flow in planetary cores and subsurface oceans. *Phys. Earth Planet. Inter.* **173** (1-2), 141–152.

OGILVIE, G.I. 2005 Wave attractors and the asymptotic dissipation rate of tidal disturbances. *J. Fluid Mech.* **543**, 19–44.

OGILVIE, G.I. 2009 Tidal dissipation in rotating fluid bodies: a simplified model. *Mon. Not. R. Astron. Soc.* **396** (2), 794–806.

PHILLIPS, O.M. 1963 Energy transfer in rotating fluids by reflection of inertial waves. *Phys. Fluids* **6** (4), 513–520.

PHILLIPS, O.M. 1966 *The Dynamics of the Upper Ocean*. Cambridge University Press.

RIEUTORD, M. 1987 Linear theory of rotating fluids using spherical harmonics part I: steady flows. *Geophys. Astrophys. Fluid Dyn.* **39** (3), 163–182.

RIEUTORD, M., GEORGEOT, B. & VALDETTARO, L. 2001 Inertial waves in a rotating spherical shell: attractors and asymptotic spectrum. *J. Fluid Mech.* **435**, 103–144.

RIEUTORD, M. & VALDETTARO, L. 1997 Inertial waves in a rotating spherical shell. *J. Fluid Mech.* **341**, 77–99.

RIEUTORD, M. & VALDETTARO, L. 2010 Viscous dissipation by tidally forced inertial modes in a rotating spherical shell. *J. Fluid Mech.* **643**, 363–394.

RIEUTORD, M. & VALDETTARO, L. 2018 Axisymmetric inertial modes in a spherical shell at low Ekman numbers. *J. Fluid Mech.* **844**, 597–634.

RIEUTORD, M., VALDETTARO, L. & GEORGEOT, B. 2002 Analysis of singular inertial modes in a spherical shell: the slender toroidal shell model. *J. Fluid Mech.* **463**, 345–360.

ROBERTS, P.H. & STEWARTSON, K. 1963 On the stability of a Maclaurin spheroid of small viscosity. *Astrophys. J.* **137**, 777–790.

STEWARTSON, K. 1966 On almost rigid rotations. Part 2. *J. Fluid Mech.* **26** (1), 131–144.

THOMAS, N.H. & STEVENSON, T.N. 1972 A similarity solution for viscous internal waves. *J. Fluid Mech.* **54** (3), 495–506.

THOMAS, P.C., TAJEDDINE, R., TISCARENO, M.S., BURNS, J.A., JOSEPH, J., LOREDO, T.J., HELFENSTEIN, P. & PORCO, C. 2016 Enceladus's measured physical libration requires a global subsurface ocean. *Icarus* **264**, 37–47.

WALTON, I.C. 1975*a* On waves in a thin rotating spherical shell of slightly viscous fluid. *Mathematika* **22** (1), 46–59.

WALTON, I.C. 1975*b* Viscous shear layers in an oscillating rotating fluid. *Proc. R. Soc. Lond.* A **344** (1636), 101–110.